Open access • Journal Article • DOI:10.1007/BF01475788

# Measurement of electroweak parameters from hadronic and leptonic decays of the $Z^{0}$ — Source link

Bernardo Adeva, O. Adriani, M. Aguilar-Benitez, H. Akbari ...+492 more authors

**Institutions:** CERN, University of Florence, Johns Hopkins University, University of Naples Federico II ...+27 more institutions

**Published on:** 01 Jun 1991 - European Physical Journal C (Springer-Verlag)

Z. Phys. C – Particles and Fields 51, 179–203 (1991)

Zeitschrift für Physik C Particles and Fields


# Measurement of electroweak parameters from hadronic and leptonic decays of the $Z^0$

L3 Collaboration

B. Adeva[15], O. Adriani[13], M. Aguilar-Benitez[23], H. Akbari[5], J. Alcaraz[23], A. Aloisio[25], G. Alverson[9], M.G. Alviggi[25], Q. An[16], H. Anderhub[39], A.L. Anderson[12], V.P. Andreev[14], T. Angolov[12], L. Antonov[34], D. Antreasyan[7], P. Arce[23], A. Arefiev[24], R.de Asmundis[25], T. Azemoon[3], T. Aziz[8], P.V.K.S. Baba[16], P. Bagnaia[30], J.A. Bakken[29], L. Baksay[35], R.C. Ball[3], S. Banerjee[8], J. Bao[5], L. Barone[30], A. Bay[17], U. Becker[12], J. Behrens[39], S. Beingessner[4], Gy.L. Bencze[10, 15], J. Berdugo[23], P. Berges[12], B. Bertucci[30], B.L. Betev[34], A. Biland[39], R. Bizzarri[30], J.J. Blaising[4], P. Blömeke[1], B. Blumenfeld[5], G.J. Bobbink[2], M. Bocciolini[13], R. Bock[1], A. Böhm[1, 15], B. Borgia[30], D. Bourilkov[34], M. Bourquin[17], D. Boutigny[4], B. Bouwens[2], J.G. Branson[31], I.C. Brock[28], F. Bruyant[15], C. Buisson[22], A. Bujak[36], J.D. Burger[12], J.P. Burq[22], J. Busenitz[35], X.D. Cai[16], M. Capell[20], F. Carbonara[25], P. Cardenal[15], F. Carminati[13], A.M. Cartacci[13], M. Cerrada[23], F. Cesaroni[30], Y.H. Chang[12], U.K. Chaturvedi[16], M. Chemarin[22], A. Chen[41], C. Chen[6], G.M. Chen[6], H.F. Chen[18], H.S. Chen[6], M. Chen[12], M.L. Chen[3], W.Y. Chen[16], G. Chiefari[25], C.Y. Chien[5], F. Chollet[4], C. Civinini[13], I. Clare[12], R. Clare[12], H.O. Cohn[26], G. Coignet[4], N. Colino[15], V. Commichau[1], G. Conforto[13], A. Contin[15], F. Crijns[2], P. Criscuolo[25], X.Y. Cui[16], T.S. Dai[12], R. D'Alessandro[13], A. Degré[15, 4], K. Deiters[12], E. Dénes[10, 15], P. Denes[29], F. DeNotaristefani[30], M. Dhina[39], D. DiBitonto[35], M. Diemoz[30], F. Diez-Hedo[15], H.R. Dimitrov[34], C. Dionisi[30], R. Divià[15], M.T. Dova[16], E. Drago[25], T. Driever[2], D. Duchesneau[17], P. Duinker[2], I. Duran[23], H. El Mamouni[22], A. Engler[28], F.J. Eppling[12], F.C. Erné[2], P. Extermann[17], R. Fabbretti[37], G. Faber[39], M. Fabre[39], S. Falciano[30], Q. Fan[16], S.J. Fan[33], O. Fackler[20], J. Fay[22], J. Fehlmann[39], T. Ferguson[28], G. Fernandez[23], F. Ferroni[30, 15], H. Fesefeldt[1], J. Field[17], F. Filthaut[2], G. Finocchiaro[30], P.H. Fisher[5], G. Forconi[17], T. Foreman[2], K. Freudenreich[39], W. Friebel[38], M. Fukushima[12], M. Gailloud[19], Yu. Galaktionov[24], E. Gallo[13], S.N. Ganguli[8], P. Garcia-Abia[23], S.S. Gau[41], D. Gele[22], S. Gentile[30], M. Glaubman[9], S. Goldfarb[3], Z.F. Gong[18], E. Gonzalez[23], A. Gordeev[24], P. Göttlicher[1], D. Goujon[17], G. Gratta[27], C. Grinnell[12], M. Gruenewald[27], M. Guanziroli[16], J.K. Guo[33], A. Gurtu[8], H.R. Gustafson[3], L.J. Gutay[36], H. Haan[1], A. Hasan[16], D. Hauschildt[2], C.F. He[33], T. Hebbeker[1], M. Hebert[31], G. Herten[12], U. Herten[1], A. Hervé[15], K. Hilgers[1], H. Hofer[39], H. Hoorani[16], L.S. Hsu[41], G. Hu[16], G.Q. Hu[33], B. Ille[22], M.M. Ilyas[16], V. Innocente[25, 15], E. Isiksal[39], H. Janssen[15], B.N. Jin[6], L.W. Jones[3], A. Kasser[19], R.A. Khan[16], Yu. Kamyshkov[24, 26], Y. Karyotakis[4, 15], M. Kaur[16], S. Khokhar[16], V. Khoze[14], M.N. Kienzle-Focacci[17], W. Kinnison[21], D. Kirkby[27], W. Kittel[2], A. Klimentov[24], A.C. König[2], O. Kornadt[1], V. Koutsenko[24, 12], R.W. Kraemer[28], T. Kramer[12], V.R. Krastev[34], W. Krenz[1], J. Krizmanic[5], K.S. Kumar[11], V. Kumar[16], A. Kunin[24], V. Lalieu[17], G. Landi[13], D. Lanske[1], S. Lanzano[25], P. Lebrun[22], P. Lecomte[39], P. Lecoq[15], P. LeCoultre[39], D. Lee[21], I. Leedom[9], J.M. LeGoff[15], L. Leistam[15], R. Leiste[38], M. Lenti[13], E. Leonardi[30], J. Lettry[39], P.M. Levchenko[14], X. Leytens[2], C. Li[18, 16], H.T. Li[6], J.F. Li[16], L. Li[39], P.J. Li[33], Q. Li[16], X.G. Li[6], J.Y. Liao[33], Z.Y. Lin[18], F.L. Linde[28], B. Lindemann[1], D. Linnhofer[39], R. Liu[16], Y. Liu[16], W. Lohmann[38], E. Longo[30], Y.S. Lu[6], J.M. Lubbers[15], K. Lübelsmeyer[1], C. Luci[15], D. Luckey[7, 12], L. Ludovici[30], X. Lue[39], L. Luminari[30], W.G. Ma[18], M. MacDermott[39], R. Magahiz[32], M. Maire[4], P.K. Malhotra[8], R. Malik[16], A. Malinin[24], C. Maña[23], D.N. Mao[3], Y.F. Mao[6], M. Maolinbay[39], P. Marchesini[39], A. Marchionni[13], B. Martin[15], J.P. Martin[22], L. Martinez-Laso[15], F. Marzano[30], G.G.G. Massaro[2], T. Matsuda[12], K. Mazumdar[8], P. McBride[11], T. McMahon[36], D. McNally[39], Th. Meinholz[1], M. Merk[2], L. Merola[25], M. Meschini[13], W.J. Metzger[2], Y. Mi[16], G.B. Mills[21], Y. Mir[16], G. Mirabelli[30], J. Mnich[1], M. Möller[1], B. Monteleoni[13], G. Morand[17], R. Morand[4], S. Morganti[30], N.E. Moulai[16], R. Mount[27], S. Müller[1], E. Nagy[10], M. Napolitano[25], H. Newman[27], C. Neyer[39], M.A. Niaz[16], L. Niessen[1], H. Nowak[38], D. Pandoulas[1], F. Plasil[26], G. Passaleva[13], G. Paternoster[25], S. Patricelli[25], Y.J. Pei[1], D. Perret-Gallix[4], J. Perrier[17], A. Pevsner[5], M. Pieri[13], D. Piccolo[25], P.A. Piroué[29], V. Plyaskin[24], M. Pohl[39], V. Pojidaev[24], N. Produit[17], J.M. Qian[3], K.N. Qureshi[16], R. Raghavan[8], G. Rahal-Callot[39], P. Razis[35], K. Read[26], D. Ren[39], Z. Ren[16], S. Reucroft[9], A. Ricker[1], S. Riemann[38], O. Rind[3], C. Rippich[28], H.A. Rizvi[16], B.P. Roe[3], M. Röhner[1], S. Röhner[1], U. Roeser[39], L. Romero[23], J. Rose[1], S. Rosier-Lees[4], R. Rosmalen[2], Ph. Rosselet[19], A. Rubbia[12], J.A. Rubio[15, 23], M. Rubio[15], W. Ruckstuhl[17], H. Rykaczewski[39], M. Sachwitz[38, 15], J. Salicio[15, 23], J.M. Salicio[23], G. Sanders[21], M.S. Sarakinos[12], G. Sartorelli[7, 16], G. Sauvage[4], A. Savin[24], V. Schegelsky[14], K. Schmiemann[1], D. Schmitz[1], P. Schmitz[1], M. Schneegans[4], H. Schopper[40], D.J. Schotanus[2], S. Shotkin[12], H.J. Schreiber[38], R. Schulte[1], S. Schulte[1], K. Schultze[1], J. Schütte[11], J. Schwenke[1], G. Schwering[1], C. Sciacca[25], I. Scott[11], R. Sehgal[16], P.G. Seiler[37], J.C. Sens[2], I. Sheer[31], D.Z. Shen[33], V. Shevchenko[24], S. Shevchenko[24], X.R. Shi[28], K. Shmakov[24], V. Shoutko[24], E. Shumilov[24], N. Smirnov[14], E. Soderstrom[29], A. Sopczak[31], C. Spartiotis[5], T. Spickermann[1], B. Spiess[39], P. Spillantini[13],

R. Starosta[1], M. Steuer[7, 12], D.P. Stickland[29], F. Sticozzi[12], W. Stoeffl[20], H. Stone[17], K. Strauch[11], B.C. Stringfellow[36], K. Sudhakar[8, 1], G. Sultanov[16], R.L. Sumner[29], L.Z. Sun[18, 16], H. Suter[39], R.B. Sutton[28], J.D. Swain[16], A.A. Syed[16], X.W. Tang[6], E. Tarkovsky[24], L. Taylor[9], C. Timmermans[2], Samuel C.C. Ting[12], S.M. Ting[12], Y.P. Tong[41], F. Tonisch[38], M. Tonutti[1], S.C. Tonwar[8], J. Tóth[10, 15], G. Trowitzsch[38], C. Tully[27], K.L. Tung[6], J. Ulbricht[39], L. Urbán[19], U. Uwer[1], E. Valente[30], R.T. Van de Walle[2], I. Vetlitsky[24], G. Viertel[39], P. Vikas[16], U. Vikas[16], M. Vivargent[4, 12], H. Vogel[28], H. Vogt[38], G. Von Dardel[15], I. Vorobiev[24], A.A. Vorobyov[14], An.A. Vorobyov[14], L. Vuilleumier[19], M. Wadhwa[16], W. Wallraff[1], C.R. Wang[18], G.H. Wang[28], J.H. Wang[6], Q.F. Wang[11], X.L. Wang[18], Y.F. Wang[13], Z. Wang[16], Z.M. Wang[16, 18], A. Weber[1], J. Weber[39], R. Weill[19], T.J. Wenaus[20], J. Wenninger[17], M. White[12], C. Willmott[23], F. Wittgenstein[15], D. Wright[29], R.J. Wu[6], S.L. Wu[16], S.X. Wu[16], Y.G. Wu[6], B. Wyslouch[12], Y.Y. Xie[33], Y.D. Xu[6], Z.Z. Xu[18], Z.L. Xue[33], D.S. Yan[33], X.J. Yan[12], B.Z. Yang[18], C.G. Yang[6], G. Yang[16], K.S. Yang[6], Q.Y. Yang[6], Z.Q. Yang[33], C.H. Ye[16], J.B. Ye[39, 18], Q. Ye[16], S.C. Yeh[41], Z.W. Yin[33], J.M. You[16], M. Yzerman[2], C. Zaccardelli[27], L. Zehnder[39], P. Zemp[39], M. Zeng[16], Y. Zeng[1], D.H. Zhang[2], Z.P. Zhang[18, 16], J.F. Zhou[1], R.Y. Zhu[27], H.L. Zhuang[6], A. Zichichi[15, 16]

[1] I. Physikalisches Institut, RWTH, Aachen, FRG*
III. Physikalisches Institut, RWTH, Aachen, FRG*
[2] National Institute for High Energy Physics, NIKHEF, Amsterdam; NIKHEF-H and University of Nijmegen, Nijmegen, The Netherlands
[3] University of Michigan, Ann Arbor, Michigan, USA
[4] Laboratoire de Physique des Particules, LAPP, Annecy, France
[5] Johns Hopkins University, Baltimore, MD, USA
[6] Institute of High Energy Physics, IHEP, Beijing, China
[7] INFN-Sezione di Bologna, Italy
[8] Tata Institute of Fundamental Research, Bombay, India
[9] Northeastern University, Boston, MA, USA
[10] Central Research Institute for Physics of the Hungarian Academy of Sciences, Budapest, Hungary
[11] Harvard University, Cambridge, MA, USA
[12] Massachusetts Institute of Technology, Cambridge, MA, USA
[13] INFN Sezione di Firenze and University of Firenze, Italy
[14] Leningrad Nuclear Physics Institute, Gatchina, USSR
[15] European Laboratory for Particle Physics, CERN, Geneva, Switzerland
[16] World Laboratory, FBLJA Project, Geneva, Switzerland
[17] University of Geneva, Geneva, Switzerland
[18] University of Science and Technology of China, Hefei, China
[19] University of Lausanne, Lausanne, Switzerland
[20] Lawrence Livermore National Laboratory, Livermore, CA, USA
[21] Los Alamos National Laboratory, Los Alamos, NM, USA
[22] Institut de Physique Nucléaire de Lyon, IN2P3-CNRS/Université Claude Bernard, Villeurbanne, France
[23] Centro de Investigaciones Energeticas, Medioambientales y Tecnologicas, CIEMAT, Madrid, Spain
[24] Institute of Theoretical and Experimental Physics, ITEP, Moscow, USSR
[25] INFN-Sezione di Napoli and University of Naples, Italy
[26] Oak Ridge National Laboratory, Oak Ridge, TN, USA
[27] California Institute of Technology, Pasadena, CA, USA
[28] Carnegie Mellon University, Pittsburgh, Pennsylvania, PA, USA
[29] Princeton University, Princeton, NJ, USA
[30] INFN-Sezione di Roma and University of Roma, "La Sapienza", Italy
[31] University of California, San Diego, CA, USA
[32] Union College, Schenectady, NY, USA
[33] Shanghai Institute of Ceramics, SIC, Shanghai, China
[34] Central Laboratory of Automation and Instrumentation, CLANP, Sofia, Bulgaria
[35] University of Alabama, Tuscaloosa, AL, USA
[36] Purdue University, West Lafayette, IN, USA
[37] Paul Scherrer Institut, PSI, Würenlingen, Switzerland
[38] Institut für Hochenergiephysik, Zeuthen, FRG*
[39] Eidgenössische Technische Hochschule, ETH Zürich Switzerland
[40] University of Hamburg, FRG
[41] High Energy Physics Group, Taiwan, China

Received 18 February 1991

* Supported by the German Bundesministerium für Forschung und Technologie

**Abstract.** We have studied the reactions $e^+e^- \to$ hadrons, $e^+e^-$, $\mu^+\mu^-$ and $\tau^+\tau^-$, in the energy range $88.2 \leqq \sqrt{s} \leqq 94.2$ GeV. A total luminosity of 5.5 pb$^{-1}$, corresponding to approximately 115000 hadronic and 10000 leptonic $Z^0$ decays, has been recorded with the L3 detector. From a simultaneous fit to all of our measured cross section data, we obtain assuming lepton universality:

$M_Z = 91.181 \pm 0.010 \pm 0.02$ (LEP) GeV,

$\Gamma_Z = 2501 \pm 17$ MeV,

$\Gamma_{\text{had}} = 1742 \pm 19$ MeV, $\quad \Gamma_l = 83.6 \pm 0.8$ MeV.

If we do not assume lepton universality, we obtain for the partial decay widths of the $Z^0$ into $e^+e^-$, $\mu^+\mu^-$ and $\tau^+\tau^-$:

$\Gamma_e = 83.3 \pm 1.1$ MeV, $\quad \Gamma_\mu = 84.5 \pm 2.0$ MeV,

$\Gamma_\tau = 84.0 \pm 2.7$ MeV.

From the measured ratio of the invisible and the leptonic decay widths of the $Z^0$, we determine the number of light neutrino species to be $N_\nu = 3.05 \pm 0.10$. We include our measurements of the forward-backward asymmetry for the leptonic channels in a fit to determine the vector and axial-vector neutral current coupling constants of charged leptons to the $Z^0$. We obtain $\bar{g}_V = -0.046^{+0.015}_{-0.012}$ and $\bar{g}_A = -0.500 \pm 0.003$. In the framework of the Standard Model, we estimate the top quark mass to be $m_t = 193^{+52}_{-69} \pm 16$ (Higgs) GeV, and we derive a value for the weak mixing angle of $\sin^2\theta_W \equiv 1 - (M_W/M_Z)^2 = 0.222 \pm 0.008$, corresponding to an effective weak mixing angle of $\sin^2\bar{\theta}_W = 0.2315 \pm 0.0025$.

## 1 Introduction

Precise measurements of the production cross section of the $Z^0$ in $e^+e^-$ reactions and the hadronic and leptonic decay rates are important steps towards understanding the electroweak interaction which is very successfully described by the Standard Model [1].

The successful operation of LEP [2] in 1990 has enabled us to collect a total luminosity of 5.5 pb$^{-1}$ with the L3 detector in the energy range $88.2 \leqq \sqrt{s} \leqq 94.2$ GeV around the $Z^0$ peak. This represents approximately 115000 hadronic and 10000 leptonic $Z^0$ decays.

Earlier results on the hadronic and leptonic $Z^0$ cross sections and leptonic forward-backward asymmetries have been reported by the LEP experiments [3–6]. This analysis represents a factor of two increase in statistics with respect to our previous results [3–5]. An improved understanding of our detector has enabled us to significantly reduce the systematic uncertainties in our measurements.

In this article we present the results of the measurements of the reactions:

1. $e^+e^- \to$ hadrons,
2. $e^+e^- \to \mu^+\mu^-(\gamma)$,
3. $e^+e^- \to \tau^+\tau^-(\gamma)$,
4. $e^+e^- \to e^+e^-(\gamma)$.

We perform simultaneous fits to our measurements of these reactions in order to determine the values of various electroweak parameters.

From the shape of the cross sections around the $Z^0$ peak we obtain precise values of the mass, the total width, the hadronic and leptonic partial decay widths of the $Z^0$ and the corresponding branching ratios. The difference between the total decay width and the sum of all observed partial decay widths gives the invisible width from which the number of light neutrino families is determined. A comparison of the partial decay widths of the $Z^0$ into electrons, muons and taus permits a test of the lepton universality of the weak neutral current interaction.

Including the measurements of the forward-backward asymmetries of the leptonic reactions, we determine the vector and axial-vector couplings of the leptons. In the framework of the Standard Model we can express our results in terms of the weak mixing angle or the mass of the top quark.

The structure of this article is as follows: in Sect. 2 we describe briefly the L3 detector, the luminosity measurement is discussed in Sect. 3, the analysis of reactions 1–4 is described in Sect. 4–7. The determination of the electroweak parameters is presented in Sect. 8, and we conclude in Sect. 9.

## 2 The L3 detector

The L3 detector is designed to measure electrons, photons, muons and hadrons produced in $e^+e^-$ reactions with good spatial and energy resolution. Starting from the interaction point, the L3 detector is composed of the following subdetector systems:

- a time expansion chamber (TEC) for tracking charged particles;
- an electromagnetic calorimeter composed of bismuth germanium oxide (BGO) crystals;
- a cylindrical array of 30 scintillation counters;
- a hadron calorimeter with uranium absorber and proportional wire chamber readout;
- a muon spectrometer consisting of multi-wire drift chambers;
- a luminosity monitor composed of BGO crystal arrays on either side of the detector.

These detectors are installed in a 12 m inner diameter solenoidal magnet which provides a uniform magnetic field of 0.5 T along the beam direction. A detailed description of the detector and its performance is given in [7].

The $e^+e^-$ interactions 1–4 are recorded in the L3 detector if at least one of the following trigger requirements is fulfilled:

*Energy trigger:* At least 10 GeV is registered in the BGO calorimeter, or 15 GeV in the BGO and barrel hadron calorimeter, or 20 GeV in all calorimeters (including the end-cap calorimeters).
*Dimuon trigger:* At least two tracks are detected in the muon chambers in non-adjacent octants and at least one scintillation counter has fired.
*Single muon trigger:* At least one track with a transverse momentum greater than 1.5 GeV is detected in the muon chambers and at least one scintillation counter has fired.
*Charged track trigger:* At least two tracks with a transverse momentum greater than 0.15 GeV and with an angular separation greater than 120° in the transverse plane are observed in the TEC.
*Scintillation counter trigger:* At least five out of the 30 barrel scintillation counters fire within 13 ns of the beam gate and at least one pair of the counters hit is separated by more than 45° in azimuth.

These trigger requirements have a very large redundancy. Typically at least two trigger requirements are fulfilled by each of the reactions 1–4. This allows a check of the trigger efficiency of the individual triggers. The combined trigger efficiency for all of the above reactions is larger than 99.9%.

The response of the L3 detector is modelled with the GEANT3 [8] detector simulation program which includes the effects of energy loss, multiple scattering and showering in the detector materials and in the beam pipe. Hadronic showers in the calorimeters are simulated with the GHEISHA [9] program. Generated events are passed through the detector simulation program and are reconstructed by the same program that is used to reconstruct the data for each of the physical processes studied. The database, which keeps track of the detector status, is used in the reconstruction of simulated events to compensate for time dependent detector inefficiencies. Except where explicitly stated, all Monte Carlo studies mentioned in this article are made with events which have been tracked through the detector by the simulation program.

The right-handed coordinate system that we use to decribe the detector is defined as follows: the $z$ axis is along the direction of the incoming $e^-$, the $y$ axis is vertical and the $x$ axis points towards the center of LEP. The polar angle $\theta$ is determined with respect to the $z$ axis, and the azimuthal angle $\phi$ is determined in the $xy$ plane with respect to the $x$ axis.

In the analysis we use the following Monte Carlo event generation programs: BABAMC [10] and BHLUMI V1.22 [11] for $e^+e^- \to e^+e^-(\gamma)$ events; NGAMMA [12] for $e^+e^- \to \gamma\gamma(\gamma)$ events; JETSET 7.2 [13] and HERWIG 4.2 [14] for $e^+e^- \to$ hadrons events; KORALZ [15] for $e^+e^- \to \mu^+\mu^-(\gamma)$ and $e^+e^- \to \tau^+\tau^-(\gamma)$ events; and DIAG36 [16] for four-fermion final states.

## 3 Luminosity

The luminosity is determined from the measured rate of small-angle Bhabha scattering, $e^+e^- \to e^+e^-(\gamma)$. We describe the determination of the luminosity in detail since this measurement is crucial to the cross section measurements which we present later.

### 3.1 Luminosity monitor and trigger

The luminosity monitor consists of two electromagnetic calorimeters and two sets of proportional wire chambers, situated symmetrically on either side of the interaction point. Each calorimeter is a finely segmented and azimuthally symmetric array of 304 BGO crystals covering the polar angular range $24.93 < \theta$ or $(\pi - \theta) < 69.94$ mrad (with respect to the interaction point $x = y = z = 0$). Each crystal is read out by a photodiode and has an LED to monitor its stability. The analog photodiode signals are used for the luminosity triggers, and the digitized photodiode signals are used to determine the energy deposited in the crystals. The energy resolution of the calorimeters is about 2% at 45 GeV, and the position resolution is 0.4 mrad in $\theta$ and 0.5° in $\phi$.

Luminosity triggers are based on the analog sums of the crystal signals in a 22.5° azimuthal region. Three triggers are constructed from the $2 \times 16$ analog sums:

*Back-to-back-trigger:* At least 15 GeV is deposited in opposite 45° $\phi$ sectors of the calorimeters.
*Asymmetric double-tag trigger:* At least 25 GeV is deposited in one calorimeter and at least 5 GeV in the other.
*Prescaled single-tag trigger:* At least 30 GeV is deposited in one of the calorimeters.

Selected Bhabha events must satisfy the back-to-back trigger or the asymmetric double-tag trigger. The single-tag trigger is used to determine the trigger efficiency for Bhabha events, which is found to be $(99.9 \pm 0.1)\%$, with fill-to-fill variations of less than 0.1%.

### 3.2 Event selection

The Bhabha event selection is based on the energy deposits in the two calorimeters. A typical Bhabha event is shown in Fig. 1. Adjacent crystals with more than

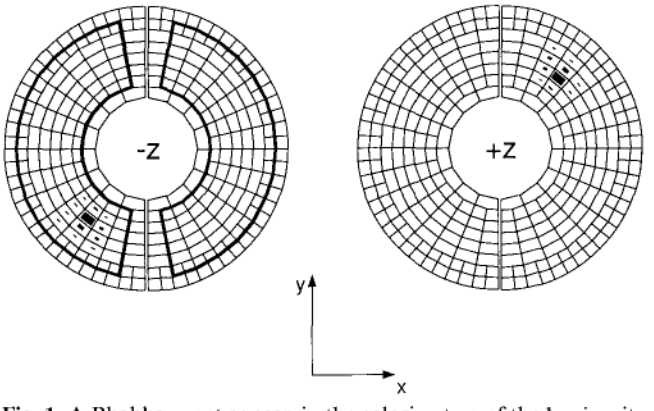


**Fig. 1.** A Bhabha event as seen in the calorimeters of the luminosity monitor. Only energy deposits exceeding 250 MeV are shown. The size of each dark box is proportional to the energy deposit in the corresponding crystal. The tight fiducial volume corresponds to the outline shown in bold for the $-z$ calorimeter

250 MeV of deposited energy are joined into clusters. The $\theta$ and $\phi$ impact coordinates of the cluster are determined from the observed energy sharing among the crystals. This is done by using a fitting function derived from the known average shape of electromagnetic showers. The same method is used to estimate the energy, $E$, of the incident particle by correcting the observed energy for lateral losses.

For most luminosity triggers one cluster is found in each calorimeter. For the events with multiple clusters we must differentiate between events with contributions from spurious beam-gas interactions and genuine radiative events. To do this, the clusters are ordered by energy and a vectorial sum of the individual cluster coordinates $(E, \theta, \phi)$ is made. The summing is stopped when the difference between the energy of the cluster and the beam energy is minimal.

Two separate samples of Bhabha events are maintained. In the first (second) sample, a tight fiducial volume cut, as described in (1) below, is imposed on the calorimeter on the $+z(-z)$ side. The criteria used for selecting luminosity events are:

1. The cluster is required to have the reconstructed $\theta$ and $\phi$ impact coordinates more than one crystal away from the calorimeter edges (see Fig. 1):

a. $30.92 < \theta < 64.41$ mrad;

b. $|\phi - 90°| > 11.25°$ and $|\phi - 270°| > 11.25°$.

We impose no restrictions on the reconstructed impact coordinates on the opposite side.

2. The reconstructed energy on one side must be greater than $0.8\,E_{\text{beam}}$ and the reconstructed energy on the other side must be greater than $0.4\,E_{\text{beam}}$.

3. The coplanarity angle, $\Delta\phi$, of the two clusters must satisfy: $|\Delta\phi - 180°| < 10°$.

The asymmetric energy cut ensures that the acceptance is not sensitive to the effect of a few dead crystals, and in addition retains most of the radiative Bhabha events. Almost all the background from random beam-gas coincidences has energies less than $0.8\,E_{\text{beam}}$ in each calorimeter and is, therefore, substantially reduced by requirement 2.

The coplanarity requirement is used to further suppress beam related background. The sidebands of the coplanarity distribution, $10° < |\Delta\phi - 180°| < 30°$, are used to subtract, on a fill-by-fill basis, the remaining background in the signal region. The residual background level of 0.2% is mainly due to random coincidences of beam-gas interactions. We assign a 0.1% systematic uncertainty to the background subtraction procedure.

The average of the two Bhabha event samples is used to calculate the luminosity. The asymmetric fiducial volume cut greatly reduces the systematic effect on the luminosity measurement due to calorimeter misalignments and/or $e^+e^-$ interaction point displacements. For example, a 2 mm displacement or a 1 mrad tilt of one calorimeter relative to the beam line increases the measured luminosity by only 0.1%. The collinearity of the Bhabha events is used to monitor relative displacements of the beam with a precision of 0.1 mm. The fill-to-fill variations of these displacements are less than 0.5 mm.

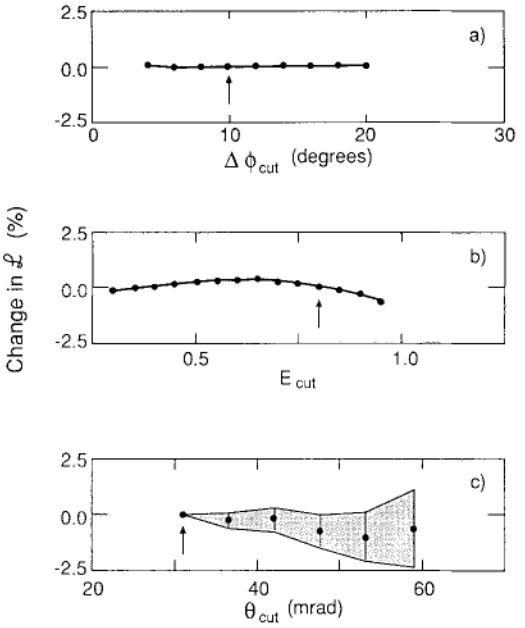


**Fig. 2a–c.** The relative change in the integrated luminosity as a function of **a** the coplanarity cut, $|\Delta\phi - 180°| < \Delta\phi_{\text{cut}}$; **b** the energy cut, one energy larger than $E_{\text{cut}}\,E_{\text{beam}}$ and the other energy larger than $\frac{1}{2}E_{\text{cut}}\,E_{\text{beam}}$; and **c** the tight fiducial volume cut, $\theta_{\text{cut}} < \theta < 64.41$ mrad. The shaded region in Fig. c indicates the statistical uncertainty (dominated by the Monte Carlo simulation) with respect to the nominal cut value. These nominal cut values are indicated by the arrows

The effect of changes in the selection requirements on the integrated luminosity, $\mathscr{L}$, is shown in Fig. 2. The relatively large statistical uncertainty on the effect of varying the fiducial volume cut is due to the fact that an increase of the minimum scattering angle allowed strongly reduces the number of selected events. On the contrary, variations of the energy and coplanarity cuts hardly change the number of selected events. Within the statistical uncertainty, the value of $\mathscr{L}$ is stable against changes in the coplanarity, energy and fiducial volume cuts. Based on Fig. 2, a 0.5% systematic uncertainty is assigned to $\mathscr{L}$ due to the event selection criteria.

### *3.3 Theoretical cross section*

To determine the visible cross section, $e^+e^- \to e^+e^-(\gamma)$ events are generated at $\sqrt{s} = 91.18$ GeV using BABAMC [10]. At the generator level, the polar angles of the scattered electron and positron are required to be in the range $0.020 < \theta < \pi - 0.020$ rad. The generated events are passed through the L3 detector simulation program. For center of mass energies, $\sqrt{s}$, off the $Z^0$ peak the visible cross section is rescaled by $(91.18\text{ GeV})^2/s$. Small $\sqrt{s}$ dependent electroweak interference effects ($\leqq 0.2\%$) are also taken into account [17]. The contribution from

$e^+e^- \to e^+e^-\gamma$ event configurations with the electron or the positron polar angle below 0.020 rad is estimated to be $(0.06 \pm 0.02)\%$.

The difference between the BABAMC and the BHLUMI V1.22 [11] predictions for the visible cross section is $(0.7 \pm 0.2)\%$. The difference between this value and the $(2 \pm 1)\%$ quoted in [4] is due, apart from increased Monte Carlo statistics, to an improved numerical integration in the initialization phase of BABAMC. The BABAMC Monte Carlo program is favored because it simulates the complete $e^+e^- \to e^+e^-(\gamma)$ phase space of experimental interest.

BABAMC is an $\mathcal{O}(\alpha)$ Monte Carlo event generator. To estimate the effect of higher order contributions, we use an analytic calculation of the leading log $\mathcal{O}(\alpha^2)$ contribution [18]. For our angular range this yields a 0.4% increase of the visible cross section with respect to the $\mathcal{O}(\alpha)$ result. The authors of [18] estimate the effect of the remaining higher order contributions to be less than 0.5%.

The event selection does not differentiate between $e^\pm$ and $\gamma$. Thus, the contribution from the $e^+e^- \to \gamma\gamma(\gamma)$ process (0.02%) must be added to the visible cross section [12]. The small background from the double-tag mode of the two-photon process, $e^+e^- \to e^+e^-X$, is generally not coplanar and is therefore accounted for by the $\Delta\phi$ sideband background subtraction procedure.

Including all contributions, the visible cross section at the $Z^0$ peak is 88.5 nb. The systematic uncertainty in the visible cross section due to the limited Monte Carlo statistics is 0.3%. We estimate a theoretical uncertainty, resulting from the approximations used in the BABAMC calculation and the effect of higher order terms beyond the leading log $\mathcal{O}(\alpha^2)$ term of 0.5% [18]. The geometry of the calorimeters has been measured by survey and has been checked independently using the proportional wire chambers mounted in front of the calorimeters. The uncertainty in the geometry measurements introduces a 0.4% systematic uncertainty in the visible cross section.

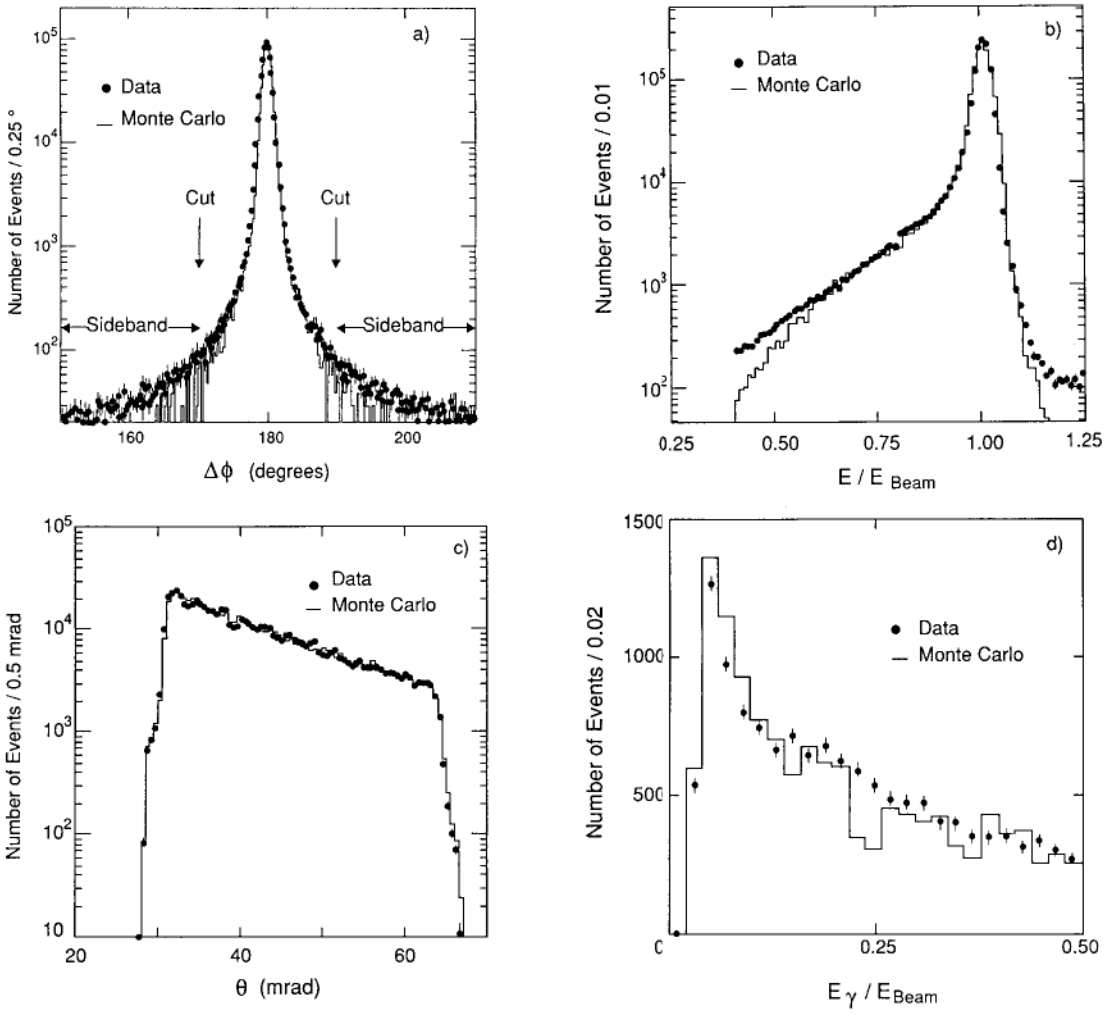


**Fig. 3a–d.** **a** The observed coplanarity distribution, $\Delta\phi$. The cuts used to select Bhabha events, $|\Delta\phi - 180°| < 10°$, and the sidebands used for the background subtraction are indicated in the figure. **b** Distribution of the observed energies normalized to the beam energy. **c** Distribution of the observed polar scattering angle, $\theta$. The wiggles in this distribution are due to the changing angular resolution across the face of each crystal. **d** Distribution of the observed photon energies. All four distributions are compared to the Monte Carlo simulations. The Monte Carlo sample is ten times smaller than the data sample

**Table 1.** Breakdown of the contributions to the systematic uncertainty in the luminosity measurement. The total systematic uncertainty is the quadratic sum of the various contributions

| Source of sytematic uncertainty | Contribution to $\Delta\mathscr{L}(\%)$ |
|---|---|
| Luminosity trigger | 0.1 |
| Geometry of the calorimeters | 0.4 |
| Bhabha event selection criteria | 0.5 |
| Background subtraction | 0.1 |
| Monte Carlo statistics | 0.3 |
| Total experimental systematic uncertainty | 0.7 |
| Theoretical systematic uncertainty | 0.5 |
| Total systematic uncertainty | 0.9 |

### *3.4 Luminosity measurement*

Approximately $5\times10^5$ events from the $2\times10^6$ recorded luminosity triggers pass the event selection criteria described above. The measured coplanarity distribution, after the energy and the fiducial volume cuts, is compared to the Monte Carlo prediction in Fig. 3a. Figures 3b–c show the measured energy and $\theta$ distributions for the selected Bhabha sample, together with the Monte Carlo predictions. Only the statistical errors on the data are shown; the statistical errors on the Monte Carlo simulation are three times as large as those on the data. Apart from the tails of the energy distribution, the three distributions are in good agreement with the Monte Carlo simulations. The excess of data events at high energies is due to real Bhabha interactions contaminated with a spurious beam-gas interaction. The origin of the small excess at low energies is either due to the limitations of the detector simulation program, the beam-gas interactions or the $\mathscr{O}(\alpha)$ nature of the BABAMC event generator; its effect on the value of the integrated luminosity is less than 0.3%.

Radiative Bhabha events are used to further investigate the quality of the Monte Carlo simulation. The $\gamma$ is identified as the smaller energy cluster in events with two separate clusters in one calorimeter. Requiring the $\gamma$ energy, $E_\gamma$, to be larger than $0.05\,E_{\text{beam}}$, about $1.5\times10^4$ radiative Bhabha events are identified. Figure 3d shows the measured $E_\gamma$ distribution and the Monte Carlo prediction. The agreement is satisfactory.

The various contributions to the systematic uncertainty in the luminosity are summarized in Table 1. The total systematic error of 0.9% is obtained by adding in quadrature the different contributions.

At the $Z^0$ peak, our visible Bhabha cross section is more than twice the $e^+e^-\to$hadrons cross section. Therefore, the statistical uncertainty in the luminosity measurement is small compared with that of any $Z^0$ decay channel. For the investigated $Z^0$ decay channels we list for each center of mass energy point the corresponding integrated luminosity in Tables 2, 3, 5 and 7.

## 4 $e^+e^-\to$hadrons

The primary triggers for $e^+e^-\to$hadrons events are the energy, scintillation counter, and charged track triggers. In addition, events with muons are also triggered by the single muon trigger. Since the hadronic events are triggered by three independent triggers which are largely redundant, we can determine the individual trigger efficiencies from a study of the trigger data of the selected hadronic events. This analysis shows that the calorimetric trigger is $(99.93\pm0.05)\%$ efficient, and the scintillation counter and charged track triggers are each 95% efficient. The combined trigger efficiency for hadronic events is larger than 99.9%. The systematic error due to trigger inefficiencies is negligible.

### *4.1 Event selection*

The event selection for the process $e^+e^-\to$hadrons is based on the energy depositions in the electromagnetic and hadronic calorimeters, and the momentum of muons measured in the muon chambers. The hadronic calorimeter covers 99.5% of the solid angle. A clustering algorithm is used to group energy depositions in the calorimeters [19]. The granularity and the minimum energy needed to form a cluster in the end-caps is slightly larger than in the barrel region. Therefore, these two regions are considered separately. The algorithm reconstructs on average only one cluster for each electron, photon or muon and only a few clusters for taus. A typical hadronic event contains about forty clusters. We are therefore able to reject $e^+e^-$, $\mu^+\mu^-$ and $\tau^+\tau^-$ events with a cut on the number of clusters. Hadronic events are selected using the following criteria:

1. $0.5<E_{\text{vis}}/\sqrt{s}<1.5$, where $E_{\text{vis}}$ is the total energy observed in the detector.
2. $|E_\parallel|/E_{\text{vis}}<0.5$, where $E_\parallel$ is the energy imbalance along the beam direction.
3. $E_\perp/E_{\text{vis}}<0.5$, where $E_\perp$ is the transverse energy imbalance.
4. The number of clusters, $N_{\text{cluster}}$, reconstructed in the calorimeters is required to satisfy:

a. $N_{\text{cluster}}\geqq 13$ for $|\cos\theta_t|<0.74$ (Barrel) or

b. $N_{\text{cluster}}\geqq 9$ for $|\cos\theta_t|>0.74$ (End-cap)

where $\theta_t$ is the polar angle of the event thrust axis with respect to the beam line.

Figures 4a–c show the distributions of $E_{\text{vis}}/\sqrt{s}$, $|E_\parallel|/E_{\text{vis}}$ and $E_\perp/E_{\text{vis}}$, respectively. Signal and background Monte Carlo distributions are also shown. The agreement between the data and Monte Carlo distributions is evident in the signal region. The small discrepancies outside the cuts can be attributed to various sources, e.g. beam-wall interactions, beam-gas interactions, two-photon events and cosmic ray showers. This is verified by scanning these events and by an analysis based on the number of TEC tracks and scintillation counter hits. In Fig. 5 the distributions of the number of clusters observed in the barrel and end-cap regions are shown. The distributions show good agreement between the data and the Monte Carlo simulation.

Because of the very good agreement between the measured and the simulated distributions, the systematic un-

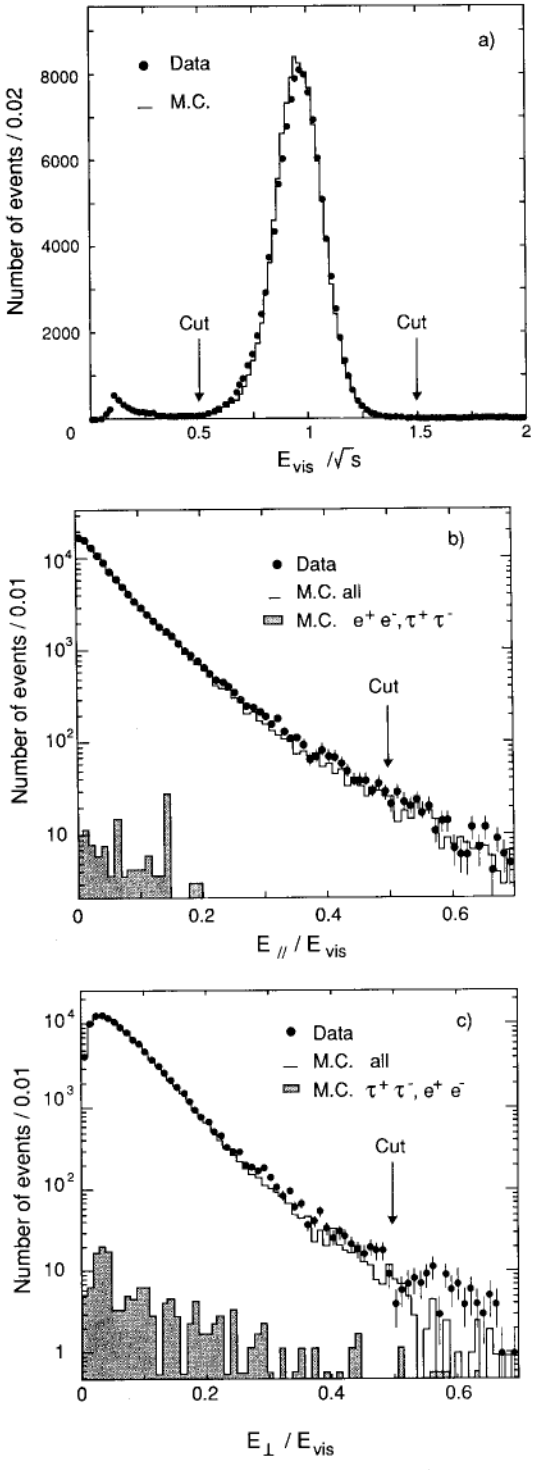


**Fig. 4a–c.** The energy distributions for $e^+e^- \rightarrow$hadrons: **a** visible energy fraction, **b** longitudinal energy imbalance, and **c** transverse energy imbalance, are compared with the same distributions for Monte Carlo signal and background events. In these figures all event selection cuts are imposed, except the cut on the variable plotted

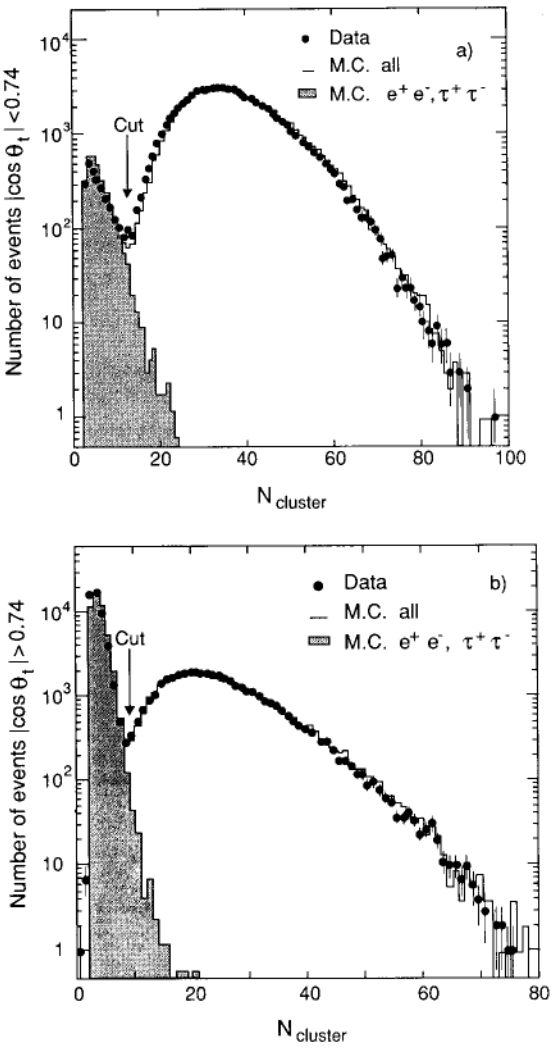


**Fig. 5a, b.** Number of clusters reconstructed in the calorimeters for hadronic events with **a** $|\cos\theta_t| < 0.74$ and **b** $|\cos\theta_t| > 0.74$, are compared with the same distributions for Monte Carlo signal and background events. In these figures all event selection cuts are imposed, except the cut on the variable plotted

certainty due to the event selection cuts is small. By varying the selection criteria we estimate a systematic uncertainty in the event selection of 0.3%.

The acceptance is determined with $e^+e^- \rightarrow$hadrons events that have been generated with the JETSET 7.2 [13] Monte Carlo program. The resulting acceptance, including detector inefficiencies, is $(99.04 \pm 0.03)\%$ for hadronic decays of the $Z^0$. A calculation of the acceptance with the HERWIG 4.2 [14] Monte Carlo program gives $(98.9 \pm 0.1)\%$. Reasonable variations of the fragmentation parameters do not affect the acceptance. The uncertainty in the effect of the inefficient regions on the acceptance is less than 0.1%. The dependence of the acceptance on $\sqrt{s}$ is of order 0.1% in the region of interest. From these studies we estimate that the systematic error on the acceptance is 0.2%.

An analysis of simulated $e^+e^- \rightarrow \tau^+\tau^-(\gamma)$ events yields a background contamination in the hadronic event sample of $(0.10 \pm 0.02)\%$. The $e^+e^- \rightarrow e^+e^-(\gamma)$ process introduces a background of approximately 7 pb, which corresponds to 0.02% on the $Z^0$ peak. The requirement $E_{vis}/\sqrt{s} > 0.5$ results in a small, $\sqrt{s}$ independent, contribution from e.g. beam-gas interactions and two-photon events of about 20 pb. This is estimated by extrapolating

**Table 2.** Results on the cross section for the reaction $e^+e^- \to$ hadrons. Quoted errors are statistical only; the overall systematic uncertainty in the cross section is 0.4% (excluding the 0.9% luminosity uncertainty)

| $\sqrt{s}$ (GeV) | $N_{\text{events}}$ | $\mathscr{L}(\text{nb}^{-1})$ | $\sigma_{\text{tot}}$ (nb) |
|---|---|---|---|
| 88.224 | 1776 | 394.5 | $4.51 \pm 0.11$ |
| 89.227 | 3841 | 455.5 | $8.47 \pm 0.14$ |
| 90.227 | 6725 | 365.2 | $18.54 \pm 0.25$ |
| 91.222 | 83835 | 2791.5 | $30.31 \pm 0.12$ |
| 92.217 | 8637 | 401.4 | $21.68 \pm 0.26$ |
| 93.221 | 6368 | 519.7 | $12.33 \pm 0.16$ |
| 94.215 | 3915 | 481.8 | $8.17 \pm 0.14$ |
| Totals | 115097 | 5409.6 | |

the observed rate in the $0.2 < E_{\text{vis}}/\sqrt{s} < 0.5$ region. The measured cross sections are corrected for these background contributions.

An independent analysis of the same data has been carried out, employing a different cluster algorithm and a different event selection based on the number of clusters and the number of scintillation counter hits. The differences between the two analyses are consistent with the estimated systematic uncertainty.

### *4.2 Cross sections*

After applying the above selection criteria, 115097 events remain, which correspond to an integrated luminosity of 5.41 $\text{pb}^{-1}$. Table 2 lists the cross section for the reaction $e^+e^- \to$ hadrons as a function of the center of mass energy, along with the number of hadronic events and the integrated luminosity at each energy point. The cross sections are corrected for the finite energy spread of the LEP beams as discussed in Sect. 8.2.

Studies of the ratio of the number of events collected versus integrated luminosity as a function of time, show no evidence of significant point-to-point or time dependent systematic errors in the scan around the $Z^0$ peak.

We obtain an overall systematic error in the corrected number of hadronic events of 0.4%. This includes contributions from event selection (0.3%) and acceptance (0.2%). Combining this error in quadrature with the 0.9% systematic error on the luminosity measurement, gives an overall systematic error on the measured hadronic cross section of 1.0%.

## 5 $e^+e^- \to \mu^+\mu^-(\gamma)$

The main triggers for $e^+e^- \to \mu^+\mu^-(\gamma)$ events are the dimuon and charged track triggers. The combined trigger efficiency of these two triggers within our acceptance is found to be greater than 99.9%.

### *5.1 Event selection*

The selection of $e^+e^- \to \mu^+\mu^-(\gamma)$ events is based on the signals from the muon chambers, scintillation counters, and central tracking chamber. The selection criteria are as follows:

1. The event is required to have two tracks in the muon chambers in the fiducial volume defined by $|\cos\theta| < 0.8$ satisfying the following requirements:
   a. To match the dimuon trigger requirements, both tracks must have a measured momentum of at least 2 GeV and the acoplanarity angle between them must be less than 90°.
   b. At least one track must extrapolate to within 100 mm of the nominal vertex position in both the transverse and longitudinal planes.
2. At least one muon chamber track must have a measured momentum greater than $\frac{2}{3}E_{\text{beam}}$.
3. At least one of the scintillation counters hit by the muons must give a signal, which after correction for time of flight must be within 3 ns of the beam gate.
4. The event is required to have at least one and no more than five TEC tracks with a transverse distance of closest approach to the beam axis of less than 5 mm.

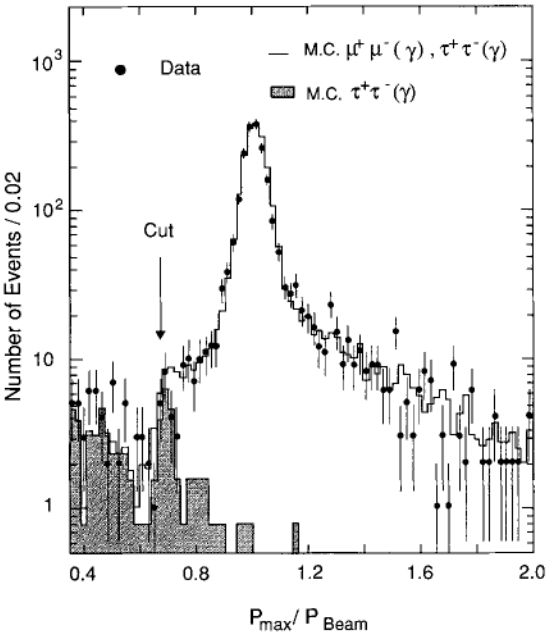


**Fig. 6.** Distribution of the maximum muon momentum in the $e^+e^- \to \mu^+\mu^-(\gamma)$ events at the $Z^0$ peak compared to the Monte Carlo simulation, including the simulation of the $e^+e^- \to \tau^+\tau^-(\gamma)$ background. In this figure all events selection cuts are imposed, except the momentum cut

Figure 6 shows the momentum distribution of the most energetic muon in the event compared to the Monte Carlo prediction, for data at the $Z^0$ peak. Good agreement between the data and the Monte Carlo is observed. The momentum cut (2) removes most of the background from $e^+e^- \to \tau^+\tau^-(\gamma)$, two-photon processes and hadronic events. The remaining $e^+e^- \to$ hadrons events are rejected by the charged track multiplicity requirement (4).

We estimate a background from $e^+e^- \to \tau^+\tau^-(\gamma)$ events of $(1.2 \pm 0.1)\%$ using events generated with KORALZ [15] and passed through the detector simu-

lation. The background from reactions such as $e^+e^- \to$ hadrons, $e^+e^- \to e^+e^-\mu^+\mu^-$, etc. is negligible. Cosmic ray background is rejected by requiring that the muons originate from the nominal vertex position (1b, 4) and that the event is in time with the bunch crossing (3). The residual cosmic ray background in the selected sample is $(0.20 \pm 0.02)\%$; this is determined using events with TEC tracks that do not pass through the interaction point. Varying the above criteria we estimate a systematic uncertainty in the cross section measurement due to the event selection of 0.5%.

To calculate the geometrical acceptance and event selection efficiency, $e^+e^- \to \mu^+\mu^-(\gamma)$ events are generated with KORALZ. For the cuts described above, the acceptance, including detector inefficiencies, is $(78.3 \pm 0.3)\%$, inside the fiducial volume. This acceptance is independent of the center of mass energy. We assign a systematic uncertainty of 0.5% to the acceptance due to imperfections in the detector simulation.

Higher order radiative corrections account for significant deviations from first order predictions in the region of the $Z^0$ peak. Thus, a good understanding of photon radiation is essential for a precise measurement of electroweak parameters. We have measured these radiative processes directly by studying $e^+e^- \to \mu^+\mu^-\gamma$ events. For each event the largest electromagnetic cluster in the BGO calorimeter is identified as the photon. Figure 7a shows the measured photon spectrum for $E_\gamma > 0.5$ GeV at the $Z^0$ peak. The effect of photon radiation can also be seen in Fig. 7b, where the acollinearity angle of the $\mu^+\mu^-$ pair is shown. In both cases the Monte Carlo correctly simulates the effects of hard photon radiation.

An alternative selection of $\mu^+\mu^-$, which employs scintillation counter timing to select good muons and calorimetric clusters to reject hadronic events, yields very similar results.

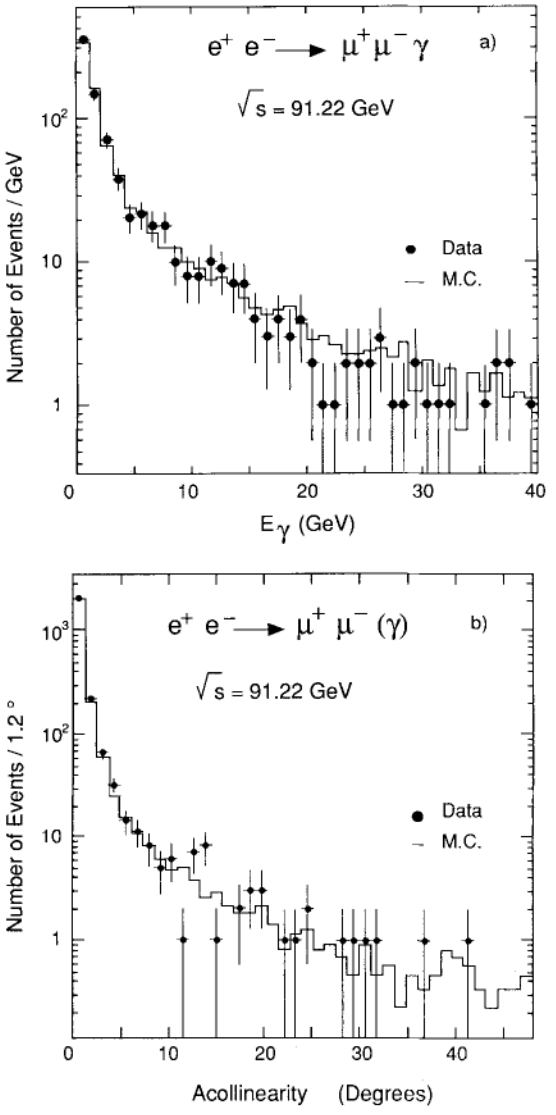


**Fig. 7a, b.** **a** The photon energy spectrum for $e^+e^- \to \mu^+\mu^-(\gamma)$ events and **b** the acollinearity distribution for $e^+e^- \to \mu^+\mu^-(\gamma)$ events. Both distributions are compared to the Monte Carlo simulations

### 5.2 *Cross sections*

After applying the above selection criteria, 3245 events are selected from the data sample with a total integrated luminosity of 5.35 $pb^{-1}$. The number of events and the luminosity collected at each energy point are listed in Table 3.

We determine the cross section in the range $|\cos\theta| < 0.8$ where the measurements are performed. Then, we extrapolate this result to the full solid angle using the KORALZ Monte Carlo program. In principle, the cross section for $|\cos\theta| < 0.8$ is sufficient for the determination of the electroweak parameters. The extrapolation of the cross section to the full solid angle facilitates comparisons among the LEP experiments. We quote both cross sections in Table 3, where $\sigma_{meas}$ is the measured cross section for $|\cos\theta| < 0.8$ and $\sigma_{tot}$ is the cross section extrapolated to the full solid angle. Both cross sections are corrected for acceptance, radiative effects and background. It should be noted that the extrapolation of the cross section includes a small correction for the energy dependence of the acceptance due to hard photon initial state radiation. The maximum vari-

**Table 3.** Results on the cross section for the reaction $e^+e^- \to \mu^+\mu^-(\gamma)$. $\sigma_{meas}$ is the acceptance corrected cross section for $|\cos\theta| < 0.8$ and $\sigma_{tot}$ is the cross section extrapolated to the full solid angle. Quoted errors are statistical only and the overall systematic uncertainty in the cross section is 0.8% (excluding the 0.9% luminosity uncertainty)

| $\sqrt{s}$ (GeV) | $N_{events}$ | $\mathscr{L}$ ($nb^{-1}$) | $\sigma_{meas}$ (nb) | $\sigma_{tot}$ (nb) |
|---|---|---|---|---|
| 88.224 | 56 | 379.0 | $0.186 \pm 0.024$ | $0.263 \pm 0.035$ |
| 89.227 | 91 | 419.2 | $0.273 \pm 0.028$ | $0.381 \pm 0.040$ |
| 90.227 | 196 | 359.9 | $0.687 \pm 0.049$ | $0.951 \pm 0.068$ |
| 91.222 | 2388 | 2812.9 | $1.072 \pm 0.022$ | $1.479 \pm 0.030$ |
| 92.217 | 257 | 387.9 | $0.837 \pm 0.052$ | $1.152 \pm 0.071$ |
| 93.221 | 144 | 503.1 | $0.361 \pm 0.030$ | $0.503 \pm 0.042$ |
| 94.215 | 113 | 484.4 | $0.293 \pm 0.027$ | $0.411 \pm 0.038$ |
| Totals | 3245 | 5346.4 | | |

ation of the acceptance is 2% in the energy range covered by our measurements. We use the extrapolated cross section, $\sigma_{\text{tot}}$, for the determination of the electroweak parameters in Sect. 8.

We estimate a total systematic uncertainty in both cross sections of 0.8% (excluding the 0.9% luminosity uncertainty); this includes uncertainties due to event selection (0.5%), acceptance and efficiency (0.5%), Monte Carlo statistics and cross section extrapolation (0.4%), and background subtraction (0.1%).

### 5.3 *Forward-backward asymmetry*

The forward-backward asymmetry, $A_{\text{FB}}$, is defined as follows:

$$A_{\text{FB}} \equiv \frac{\sigma_F - \sigma_B}{\sigma_F + \sigma_B}, \tag{1}$$

where $\sigma_F(\sigma_B)$ is the cross section for events with the $\mu^-$ scattered into the forward (backward) hemisphere with respect to the electron beam direction.

For the measurement of the $e^+e^- \to \mu^+\mu^-(\gamma)$ forward-backward asymmetry the following selection criteria are applied in addition to the above cuts 1–4:

5. The muons must have opposite charges.
6. The acollinearity angle of the $\mu^+\mu^-$ pair must be less than 15°.

3104 events in the data sample of 5.35 $\text{pb}^{-1}$ fulfill these requirements. Since one needs to distinguish $\mu^+$ and $\mu^-$ for the measurement of the asymmetry, we have checked the charge confusion by searching for events where both muons have the same charge. We find a charge confusion of $(1.2 \pm 0.2)\%$ for single muons. This charge confusion arises mainly from muons passing near the edges of the sensitive area of the muon chambers. A study of these events shows that the probability that both muon charges are wrongly measured is less than 0.2%. Only these events contribute to a wrong measurement of the forward-backward asymmetry, since the events with equal muon charges are rejected by cut 5. The systematic error due to the charge confusion is $0.004 \times A_{\text{FB}}$, which is much smaller than the statistical error of the measurement.

The acollinearity cut of 15° is applied to reduce the contribution from hard photon radiation to the differential cross section. With this cut the lowest order form of the angular distribution, $\frac{3}{8}(1+\cos^2\theta) + A_{\text{FB}}\cos\theta$, can be used for the determination of the asymmetry. Here $\theta$ is the angle between the $\mu^-$ and the $e^-$. A study with KORALZ and ZFITTER [20] (the latter is described in Sect. 8.3) shows that this form is good to within 0.6% in the $|\cos\theta| < 0.8$ angular region, corresponding to a systematic error of less than 0.003 in the asymmetry.

The asymmetry at a given energy point is determined from a maximum likelihood fit to the angular distribution. The likelihood is defined as:

$$L \equiv \prod_i \left(\tfrac{3}{8}(1+\cos^2\theta_i) + A_{\text{FB}}\cos\theta_i\right). \tag{2}$$

The product is taken over all the events selected for the asymmetry determination. This asymmetry determination is independent of variations in the acceptance as a function of $\theta$, provided that the acceptance is the same for $\mu^+$ and $\mu^-$. A comparison of the momentum distributions of positive and negative muons in the forward and backward regions shows that in each hemisphere the acceptance is charge independent to better than 0.2%. Therefore, the corresponding systematic error in the asymmetry is less that 0.002.

The very small cosmic ray background in the selected $e^+e^- \to \mu^+\mu^-(\gamma)$ event sample introduces a negligible systematic error. The only sizeable physical background is the 1.2% background from $e^+e^- \to \tau^+\tau^-(\gamma)$ events. This background does not introduce any systematic bias, since these events have an asymmetry quite similar to that of $e^+e^- \to \mu^+\mu^-(\gamma)$ events.

In summary, including the error for using the lowest order form discussed above, we assign a total systematic error of 0.005 to the measurement of the forward-backward asymmetry of $e^+e^- \to \mu^+\mu^-(\gamma)$.

The forward-backward asymmetries obtained from the maximum likelihood fit are presented in Table 4 for the different center of mass energies. As a consistency check, we also calculated $A_{\text{FB}}$ by direct counting of the events with a forward or backward scattered $\mu^-$. We corrected for the $\cos\theta$ dependent detector acceptance and extrapolated to the full solid angle using the lowest order formula for the angular distribution given above. The results are also quoted in Table 4, and they are in very good agreement with the results obtained from the maximum likelihood method. To test the validity of the approximation of the angular distribution given above, we fit the acceptance corrected $\cos\theta$ distribution for the $e^+e^- \to \mu^+\mu^-(\gamma)$ events at the $Z^0$ peak to determine $A_{\text{FB}}$. We obtain $A_{\text{FB}} = 0.01 \pm 0.02$ with a $\chi^2$ of 5.4 for 6 degrees of freedom. Figure 8 shows the acceptance corrected $\cos\theta$ distribution together with the result of the fit. We use the asymmetries obtained from the maximum likelihood method for the determination of electroweak parameters in Sect. 8.

**Table 4.** Measured forward-backward asymmetry, $A_{\text{FB}}$, of the reaction $e^+e^- \to \mu^+\mu^-(\gamma)$. Both the asymmetry determined from the number of events in the forward and backward hemispheres and the asymmetry determined using the maximum likelihood method are given. Quoted errors are statistical only. The systematic error is estimated to be 0.005

| $\sqrt{s}$ (GeV) | $A_{\text{FB}}$ | |
|---|---|---|
| | Counting | Likelihood |
| 88.224 | $-0.41 \pm 0.13$ | $-0.44 \pm 0.13$ |
| 89.227 | $-0.02 \pm 0.12$ | $-0.03 \pm 0.11$ |
| 90.227 | $-0.136 \pm 0.076$ | $-0.144 \pm 0.077$ |
| 91.222 | $0.014 \pm 0.022$ | $0.017 \pm 0.021$ |
| 92.217 | $0.100 \pm 0.066$ | $0.106 \pm 0.066$ |
| 93.221 | $0.031 \pm 0.090$ | $0.130 \pm 0.093$ |
| 94.215 | $0.122 \pm 0.098$ | $0.164 \pm 0.098$ |

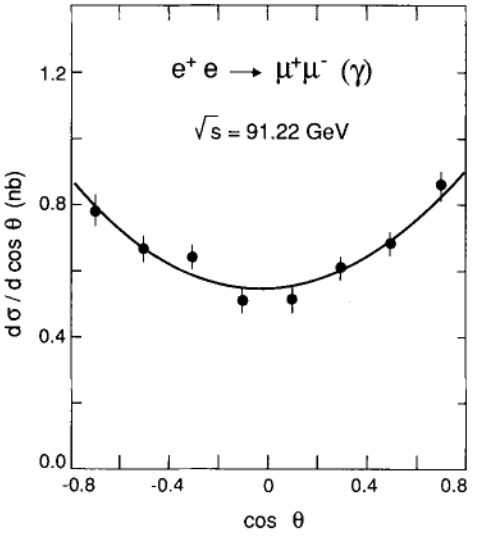


**Fig. 8.** Acceptance corrected $\cos\theta$ distribution for $e^+e^-\to\mu^+\mu^-(\gamma)$ events at the $Z^0$ peak. The solid line corresponds to the result of a $\chi^2$ fit to the functional form shown in (2)

## 6 $e^+e^-\to\tau^+\tau^-(\gamma)$

The triggers for $e^+e^-\to\tau^+\tau^-(\gamma)$ events are the energy, charged track and single muon triggers. Comparing events that have been triggered by any of the three, we find that the combined trigger efficiency is greater than 99.9%.

### *6.1 Event selection*

The $e^+e^-\to\tau^+\tau^-(\gamma)$ events are selected using all possible decay modes of the tau. The selection criteria are based on information from the electromagnetic and hadronic calorimeters, muon chambers, scintillation counters and central tracking chamber. Jets are formed by merging calorimetric clusters and muon chamber tracks. Muons must satisfy a momentum-dependent vertex cut to reject calorimeter punch-through and cosmic ray background. If the calorimetric energy deposition in the jet associated with a muon is consistent with that expected for a minimum ionizing particle, the muon is considered to be isolated.

The selection criteria are:

1. The total energy deposited in the electromagnetic calorimeter is required to be greater than 2 GeV and less than 60 GeV.
2. The number of clusters reconstructed in the electromagnetic calorimeter must be less than 13 and the number of charged tracks in the TEC must be less than 9.
3. The event is required to have at least one scintillation counter hit, which after correction for time of flight must be within 6 ns of the beam gate.
4. The event must contain at least two and at most three jets, each with an energy greater than 3 GeV.
5. The acollinearity angle between the two most energetic jets must be less than 14°.
6. The event is required to have no more than one isolated muon and, in addition, the muon must have a momentum of less than $0.88\,E_{\text{beam}}$.
7. If the shower profile of a jet is consistent with an electron or a photon, the energy deposited in the BGO associated with that jet must be less than $0.88\,E_{\text{beam}}$.

The analysis is further restricted to events which are contained within the fiducial volume defined by $|\cos\theta_t| < 0.7$, where $\theta_t$ is the polar angle of the event thrust axis. We estimate a 2.0% systematic uncertainty in the event selection by varying the above event selection cuts.

The requirement on the total energy deposited in the electromagnetic calorimeter (1) is used to remove most of the $e^+e^-\to\mu^+\mu^-(\gamma)$ and $e^+e^-\to e^+e^-(\gamma)$ events

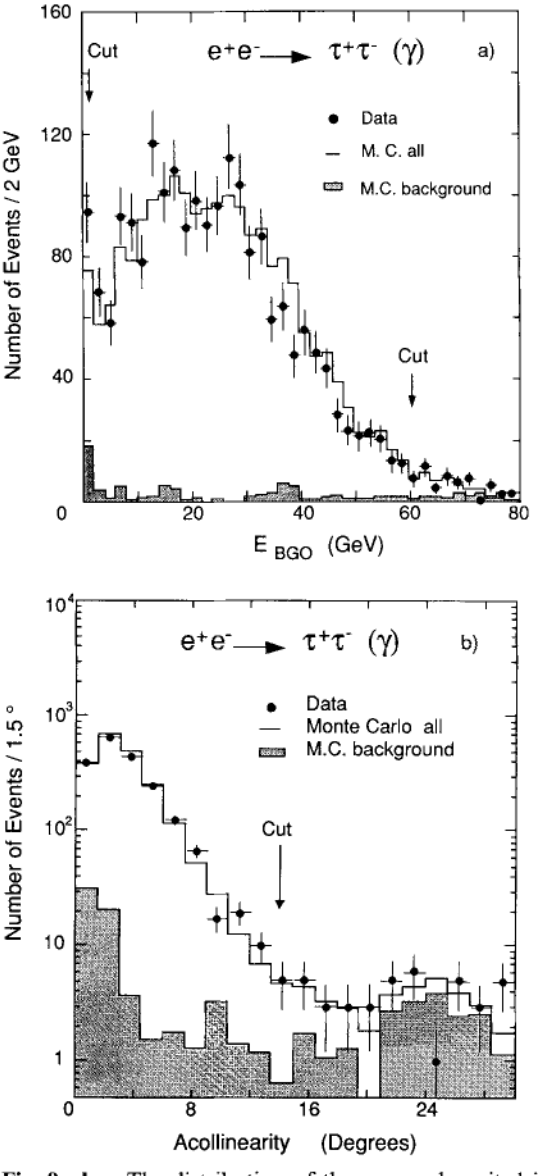


**Fig. 9a, b.** **a** The distribution of the energy deposited in the BGO calorimeter and **b** the distribution of the acollinearity for $e^+e^-\to\tau^+\tau^-(\gamma)$ events. Both distributions are compared to the Monte Carlo simulations, including background simulations for $e^+e^-\to e^+e^-(\gamma)$, $e^+e^-\to\mu^+\mu^-(\gamma)$ and $e^+e^-\to$hadrons. In these figures all event selection cuts are imposed, except the cut on the variable plotted

from the data sample. Hadronic events are suppressed by the multiplicity requirement (2), while cosmic ray background is rejected by the scintillation counter requirement (3). The jet energy cut (4) and the acollinearity cut (5) reduce the background from beam-gas interactions and two-photon processes. Residual backgrounds from $e^+e^- \to \mu^+\mu^-(\gamma)$ and $e^+e^- \to e^+e^-(\gamma)$ events are removed with requirements (6) and (7), respectively.

Figures 9a–b show the distributions of the energy deposited in the BGO calorimeter and the acollinearity angle, respectively. The distributions are compared to the Monte Carlo predictions; the agreement is good.

To determine the geometrical acceptance and event selection efficiency, $e^+e^- \to \tau^+\tau^-(\gamma)$ events are generated using KORALZ [15]. For the selection criteria described above, the acceptance including detector inefficiencies, is $(75.4 \pm 0.3)\%$ within the fiducial volume. This acceptance is independent of the center of mass energy.

Using Monte Carlo simulation we estimate an overall background of $(2.2 \pm 0.2)\%$ from $e^+e^- \to e^+e^-(\gamma)$, $e^+e^- \to \mu^+\mu^-(\gamma)$ and $e^+e^- \to$hadrons in the data sample. The background from two-photon processes (e.g. $e^+e^- \to e^+e^-\tau^+\tau^-$, $e^+e^- \to e^+e^-q\bar{q}$) is found to be about 0.1%. From a scan of the selected events, we estimate the cosmic ray background to be $(0.2 \pm 0.1)\%$.

An alternative analysis using a different set of selection cuts and a modified cluster algorithm yields very similar results.

### 6.2 Cross sections

After applying the above selection criteria, 2540 events survive in the data sample with an integrated luminosity of 5.11 $\text{pb}^{-1}$.

Extrapolarition of the measured cross section to the full solid angle is done by Monte Carlo calculations using the KORALZ program. The extrapolation leads to a 1.2% variation of the acceptance in the energy region around the $Z^0$ peak. The number of events selected at each energy point, the corresponding cross sections measured in the fiducial volume, $\sigma_{\text{meas}}$, and the cross sections extrapolated to the full solid angle, $\sigma_{\text{tot}}$, are given in Table 5. Both cross sections are corrected for the background contaminations mentioned above. We use the extrapolated cross section, $\sigma_{\text{tot}}$, for the determination of the electroweak parameters in Sect. 8.

Excluding the 0.9% luminosity uncertainty, we estimate an overall systematic uncertainty in the cross section measurement of 2.1%. This includes contributions from the event selection criteria (2.0%), the acceptance (0.7)%, and the background subtraction (0.2%).

**Table 5.** Results on the cross sections for the reaction $e^+e^- \to \tau^+\tau^-(\gamma)$. $\sigma_{\text{meas}}$ is the acceptance corrected cross section for $|\cos\theta_t| < 0.7$ and $\sigma_{\text{tot}}$ is the cross section extrapolated to the full solid angle. Quoted errors are statistical only and the overall systematic uncertainty in the cross section is 2.1% (excluding the 0.9% luminosity uncertainty)

| $\sqrt{s}$ (GeV) | $N_{\text{events}}$ | $\mathscr{L}(\text{nb}^{-1})$ | $\sigma_{\text{meas}}$ (nb) | $\sigma_{\text{tot}}$ (nb) |
|---|---|---|---|---|
| 88.224 | 36 | 338.8 | $0.137 \pm 0.023$ | $0.227 \pm 0.037$ |
| 89.227 | 83 | 406.3 | $0.266 \pm 0.029$ | $0.437 \pm 0.047$ |
| 90.227 | 138 | 320.9 | $0.561 \pm 0.047$ | $0.918 \pm 0.077$ |
| 91.222 | 1868 | 2727.7 | $0.893 \pm 0.020$ | $1.458 \pm 0.033$ |
| 92.217 | 188 | 368.1 | $0.665 \pm 0.047$ | $1.090 \pm 0.078$ |
| 93.221 | 132 | 473.5 | $0.363 \pm 0.030$ | $0.597 \pm 0.051$ |
| 94.215 | 95 | 479.2 | $0.257 \pm 0.026$ | $0.425 \pm 0.043$ |
| Totals | 2540 | 5114.5 | | |

### 6.3 Forward-backward asymmetry

For the charge of a tau we use the sum of the charges of its decay products, as measured in the TEC, unless the tau decay products include a muon, in which case the charge is inferred from the muon spectrometer. Here we assume that the two taus correspond to the two most energetic jets. For events that are used to determine the forward-backward asymmetry, the following additional requirement is applied to the sample selected by conditions 1–7 above:

8. The charge of one tau must be $+1$ and the charge of the other tau must be $-1$.

In total, 1730 tau pair events meet the selection criteria 1–8. Among these, 617 events contain a muon. Most taus removed by cut 8 have charged decay products passing through one sector of the TEC which was disconnected or through the low resolution regions close to the anode and cathode wires.

For the determination of the $e^+e^- \to \tau^+\tau^-(\gamma)$ asymmetry, we use the direction of the $\tau^-$ with respect to the electron beam direction, as determined from the event thrust axis. The acceptance corrected angular distribution, at the $Z^0$ peak, is shown in Fig. 10. A fit to this distribution, using the same angular distribution as in Sect. 5.3, $\frac{3}{8}(1+\cos^2\theta) + A_{\text{FB}}\cos\theta$, yields $A_{\text{FB}} = 0.07 \pm 0.03$ with a $\chi^2$ of 11.5 for 6 degrees of freedom.

To obtain the forward-backward asymmetries that we use in Sect. 8 for the determination of the electroweak parameters, we follow the acceptance independent maximum likelihood method as described in Sect. 5.3 for

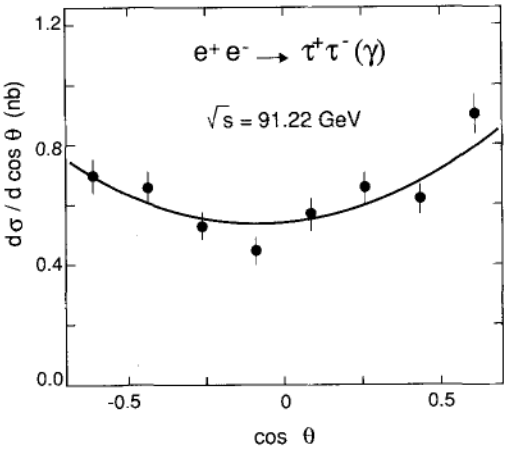


**Fig. 10.** Acceptance corrected $\cos\theta$ distribution for $e^+e^- \to \tau^+\tau^-(\gamma)$ events at the $Z^0$ peak. The solid line corresponds to the result of a $\chi^2$ fit to the functional form shown in (2)

**Table 6.** Measured forward-backward asymmetry, $A_{FB}$, of the reaction $e^+e^- \to \tau^+\tau^-(\gamma)$. Both the asymmetry determined from the number of events in the forward and backward hemispheres and the asymmetry determined using the maximum likelihood method are given. Also the asymmetry as determined from the subsample of events with a muon decay of a tau is given ($A^{\mu}_{FB}$). Quoted errors are statistical only. The systematic error is estimated to be less than 0.01

| $\sqrt{s}$ (GeV) | $A^{\mu}_{Fb}$ | $A_{FB}$ | |
|---|---|---|---|
| | likelihood | counting | likelihood |
| 88.224 | $-0.79 \pm 0.30$ | $-0.36 \pm 0.23$ | $-0.42 \pm 0.20$ |
| 89.227 | $-0.01 \pm 0.17$ | $-0.13 \pm 0.13$ | $-0.09 \pm 0.15$ |
| 90.227 | $-0.27 \pm 0.19$ | $-0.17 \pm 0.11$ | $-0.18 \pm 0.11$ |
| 91.222 | $0.04 \pm 0.05$ | $0.07 \pm 0.03$ | $0.07 \pm 0.03$ |
| 92.217 | $0.05 \pm 0.16$ | $-0.07 \pm 0.10$ | $-0.04 \pm 0.10$ |
| 93.221 | $0.02 \pm 0.19$ | $0.11 \pm 0.12$ | $0.11 \pm 0.12$ |
| 94.215 | $0.12 \pm 0.23$ | $0.12 \pm 0.13$ | $0.02 \pm 0.13$ |

$e^+e^- \to \mu^+\mu^-(\gamma)$ events. Table 6 summarizes the results obtained for the entire data sample, as well as the results obtained from the subset of events which contain a muon from the tau decay ($A^{\mu}_{FB}$). For comparison we also give in the same table the asymmetry, corrected for the $\cos\theta$ dependent detector acceptance and extrapolated to the full solid angle, obtained from direct counting of events with a forward or backward $\tau^-$. All three determinations of $A_{FB}$ agree within errors.

As a further check, the asymmetry at the $Z^0$ peak is calculated using three different samples of $e^+e^- \to \tau^+\tau^-(\gamma)$ event candidates:

- The 379 events which contain at least one tau decaying into three charged particles.
- The 1084 events contained inside the restricted fiducial volume defined by $|\cos\theta_t| < 0.6$.
- The 1559 events obtained by relaxing requirement 8 above:

The charge of one tau must be $\pm 1$. The product of the charges of the two taus must be negative or zero.

All three samples give measured asymmetries at the $Z^0$ peak consistent with the values in Table 6.

The systematic error in the asymmetry due to charge confusion in the TEC is estimated to be less than 0.008. The uncertainty in the measurement of the forward-backward asymmetry due to the cosmic ray background is estimated to be less than 0.001. The forward-backward asymmetry from the $e^+e^- \to e^+e^-(\gamma)$ background is subtracted using the Monte Carlo prediction for this asymmetry. The uncertainty due to this subtraction is estimated to be less than 0.005. We estimate the total systematic uncertainty on the asymmetry measurements to be less than 0.01.

## 7 $e^+e^- \to e^+e^-(\gamma)$

The triggers for $e^+e^- \to e^+e^-(\gamma)$ events are the energy and the charged track triggers. The combined trigger efficiency for these two independent triggers is estimated to be greater than 99.9%.

### *7.1 Event selection*

The selection of $e^+e^- \to e^+e^-(\gamma)$ events is based mainly on information from the electromagnetic calorimeter (BGO). Energy deposited in adjacent crystals is collected into clusters. Since an electromagnetic shower spreads across several crystals, we require an energy deposition in at least two crystals for a valid cluster in order to reduce the sensitivity to noise fluctuations. The selection criteria are as follows:

1. To reject hadronic events the number of clusters is required to be less than 8.
2. To reject $e^+e^- \to \tau^+\tau^-(\gamma)$ events, we require $E_{tot} > 0.7\sqrt{s}$, where $E_{tot}$ is the total electromagnetic energy.
3. To remove $e^+e^- \to \gamma\gamma(\gamma)$ events at least one track reconstructed in the TEC is required.

We further restrict the analysis to those events having the center of gravity of the two most energetic clusters in the range $44° < \theta < 136°$. Thus, we exclude events in which one or both of the two most energetic particles hit a crystal at the edge of the barrel BGO calorimeter. We also require that the acollinearity angle between the two most energetic clusters, $\zeta$, is less than 25°. Variations of the energy, acollinearity and fiducial volume cuts are used to estimate the systematic uncertainty in the event selection to be 0.4%.

Figure 11 shows the total energy measured in the electromagnetic calorimeter and Fig. 12 shows the acolli-

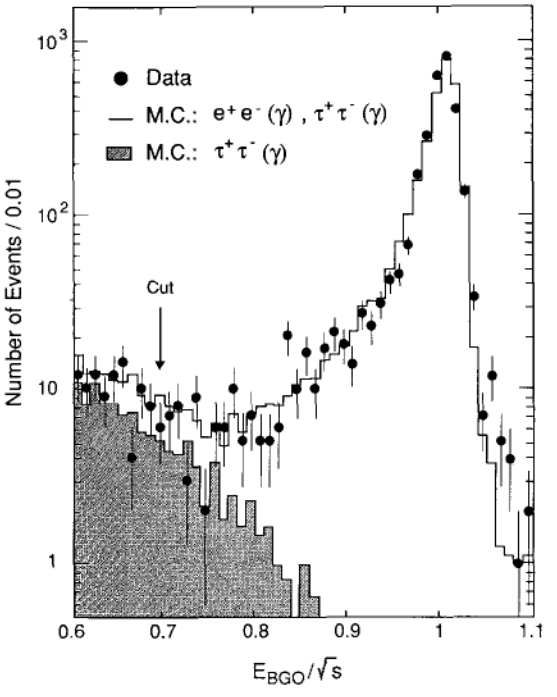


**Fig. 11.** The total energy distribution in the BGO calorimater normalized to the center of mass energy for $e^+e^- \to e^+e^-(\gamma)$ events. The distribution is compared with the Monte Carlo simulation, including the simulation of the $e^+e^- \to \tau^+\tau^-(\gamma)$ background. In this figure all event selection cuts are imposed, except the cut on the variable plotted

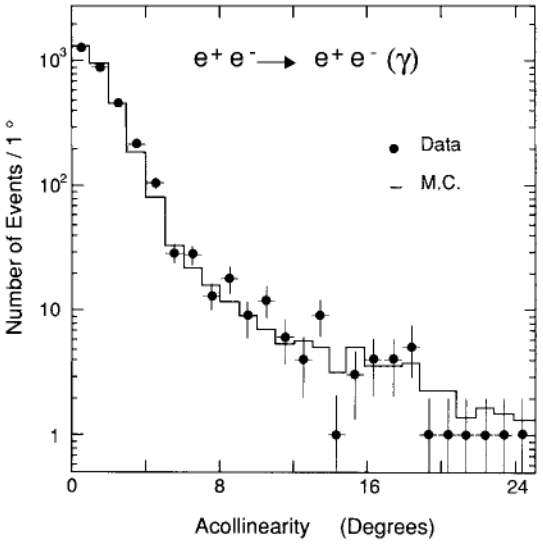


**Fig. 12.** Acollinearity distribution for $e^+e^- \to e^+e^-(\gamma)$ events compared to the Monte Carlo simulation

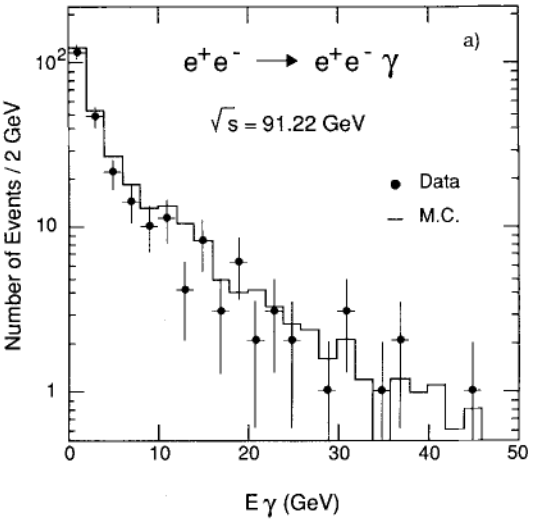


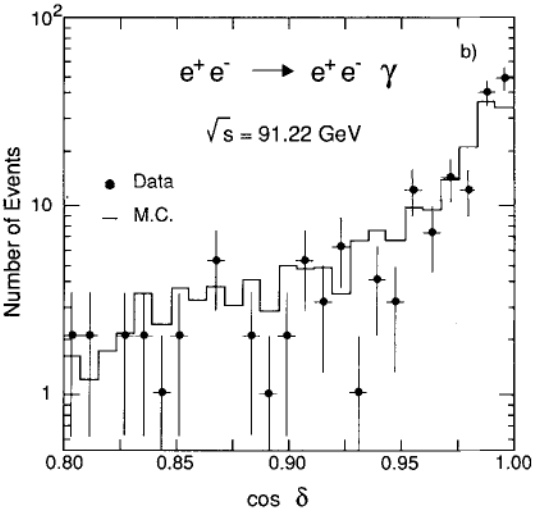


**Fig. 13a, b.** **a** The photon energy spectrum and **b** the distribution of the cosine of the angle between the photon and the nearest charged particle for $e^+e^- \to e^+e^-(\gamma)$ events. Both distributions are compared to the Monte Carlo simulations

nearity distribution of the events collected at the $Z^0$ peak. Both distributions are in good agreement with the Monte Carlo simulations.

We determine a background from $e^+e^- \to \tau^+\tau^-(\gamma)$ events of $(1.2 \pm 0.1)\%$ using events generated with KORALZ [15]. By scanning the selected events, we find that the background due to cosmic rays is negligible. The observed number of $e^+e^- \to \gamma\gamma(\gamma)$ candidates found before cut 3 is in agreement with the predicted cross section of 17.3 pb at the $Z^0$ peak [12, 21]. Background due to $\gamma$ conversions is found to be negligible, as well as the background from the two-photon process, $e^+e^- \to e^+e^-e^+e^-$.

Inside the fiducial volume and for $\zeta < 25°$, we determine the acceptance for $e^+e^- \to e^+e^-(\gamma)$ using the events generated with BABAMC [10]. We find an acceptance, including detector inefficiencies, of $(96.2 \pm 0.2)\%$. This acceptance is independent of $\sqrt{s}$, in the region of interest. The Monte Carlo prediction for the inefficiency due to dead channels in the electromagnetic calorimeter has been verified by studying events where only one electron is identified and the second one is lost in a dead region of the calorimeter. The efficiency for finding at least one track in the TEC is 99.8%. We estimate a 0.4% overall systematic uncertainty in the acceptance.

To investigate the quality of the Monte Carlo simulation for $e^+e^- \to e^+e^-(\gamma)$, we studied events in which a photon is identified. To identify a photon, we require that its energy is greater than 0.5 GeV and that the angle between it and the nearest charged particle is greater than 5°. Figure 13 shows the energy spectrum of the photon and its angular separation, $\delta$, from the nearest charged particle. Good agreement between the data and the Monte Carlo simulation, shown in the same figure, is obtained.

We performed an independent analysis with cut 2 replaced by:

$E_1 > 0.45\sqrt{s}$ and $E_2 > 2$ GeV; where $E_1$ and $E_2$ are the energies of the two most energetic clusters.

This analysis has a reduced sensitivity to the effect of the few dead crystals in the barrel BGO calorimeter. The difference between the number of events found in the two analyses, after correcting for acceptance, inefficiency and background, is 0.2%.

### *7.2 Cross sections*

After applying the above selection criteria to the data sample, we find 4175 events, corresponding to an integrated luminosity of 5.51 $pb^{-1}$. Table 7 shows the measured cross section, $\sigma_{meas}$, inside the fiducial volume for events with $\zeta < 25°$. In Fig. 14 this cross section is shown as a function of $\sqrt{s}$. The cross sections have been corrected for the background contamination mentioned above.

Excluding the 0.9% luminosity uncertainty, we assign a total experimental systematic error of 0.6% to the measured cross section. This includes uncertainties due to event

**Table 7.** Results on the cross section for the reaction $e^+e^- \to e^+e^-(\gamma)$. $\sigma_{meas}$ is the acceptance corrected cross section for $44° < \theta < 136°$ and $\zeta < 25°$. $\sigma^{GCR}$ is the acceptance corrected cross section for the GCR selection, explained in the text. Quoted errors are statistical only and the overall systematic uncertainty in the cross section is 0.6% (excluding the 0.9% luminosity uncertainty)

| $\sqrt{s}$ (GeV) | $N_{events}$ | $\mathscr{L}$(nb$^{-1}$) | $\sigma_{meas}$ (nb) | $\sigma^{GCR}$ (nb) |
|---|---|---|---|---|
| 88.224 | 123 | 381.4 | $0.337 \pm 0.030$ | $0.298 \pm 0.028$ |
| 89.227 | 243 | 468.0 | $0.539 \pm 0.034$ | $0.508 \pm 0.033$ |
| 90.227 | 303 | 360.6 | $0.866 \pm 0.050$ | $0.818 \pm 0.047$ |
| 91.222 | 2929 | 2901.3 | $1.035 \pm 0.019$ | $0.965 \pm 0.018$ |
| 92.217 | 267 | 399.2 | $0.686 \pm 0.042$ | $0.637 \pm 0.040$ |
| 93.221 | 207 | 507.2 | $0.419 \pm 0.029$ | $0.386 \pm 0.028$ |
| 94.215 | 103 | 489.7 | $0.216 \pm 0.021$ | $0.170 \pm 0.019$ |
| Totals | 4175 | 5507.4 | | |

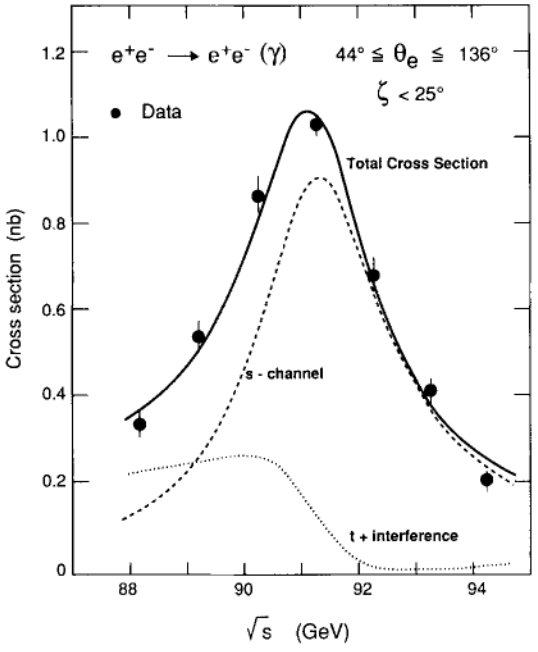


**Fig. 14.** The cross section for $e^+e^- - e^+e^-(\gamma)$ events as a function of $\sqrt{s}$. The solid line is a Standard Model prediction obtained from ALIBABA, adapted to the fit results given in Table 11. The separate $s$, and non-$s$-channel contributions are indicated

selection (0.4%), acceptance (0.4%), Monte Carlo statistics (0.2%) and background subtraction (0.1%).

As in our previous analysis [5], we also determine the cross section of the $e^+e^- \to e^+e^-(\gamma)$ process under more restrictive conditions to allow the comparison with the results of the analytical calculation by Greco found in [22] and implemented in the Caffo-Remiddi program [17]. In addition to the selection criteria 1–3, the $e^+e^- \to e^+e^-(\gamma)$ events used for the evaluation of the cross section must have an acollinearity $\zeta < 5°$ and they should contain no photons with $E_\gamma > 3.8$ GeV and $\delta > 5°$. In Table 7 the resulting values of the cross section are shown under the heading $\sigma^{GCR}$. The details of this particular selection can be found in [5].

### *7.3 Forward-backward asymmetry*

For the determination of the forward-backward asymmetry of $e^+e^- \to e^+e^-(\gamma)$, we use the polar angle of the scattered $e^-$. Due to the non-$s$-channel contributions to this process (see Sect. 7.4) we only determine the asymmetry, $A_{FB}$, by direct counting of the events in the $44° < \theta < 136°$ angular range. We correct for the $\cos\theta$ dependent acceptance in this range, but do not extrapolate our result to the full solid angle.

The polar angle of the scattered $e^\pm$ is measured by the BGO calorimeter with an angular resolution of 1.2°. The angular resolution is dominated by the longitudinal extension of the LEP bunches of about $\pm 8$ mm. The intrinsic resolution of the BGO is about 0.7 mm, which corresponds to an angular resolution of 0.07° for a point-like source. The charges of the outgoing particles are measured by the TEC. We have stringent requirements on the quality of the TEC tracks to minimize charge confusion. For each electron, the fit must include at least 30 of the possible maximum of 62 measured points and it must have a confidence level greater than 1%. The momentum resolution of the tracks satisfying these cuts is 60% at 45 GeV. If the two tracks do not satisfy the above requirements or if they have the same charge, a common circle fit through all the measured points is performed. The confidence level of this common circle fit must be at least 1%. In total 2691 events meet the additional requirements on the measured charges of the outgoing particles.

To determine the accuracy of the TEC charge assignment, we apply the same TEC track selection criteria to the selected $e^+e^- \to \mu^+\mu^-(\gamma)$ event sample and compare the charges assigned to a track by the TEC and the muon spectrometer. We find that the probability that both charges measured in the TEC are opposite to those measured in the muon chambers is $(3.5 \pm 0.5)$%. This

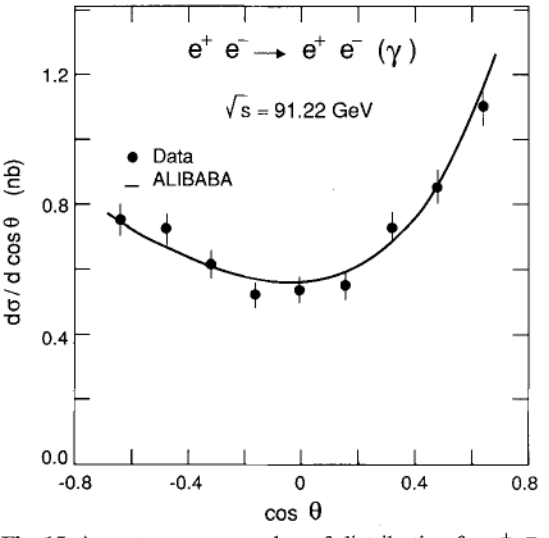


**Fig. 15.** Acceptance corrected $\cos\theta$ distribution for $e^+e^- - e^+e^-(\gamma)$ events at the $Z^0$ peak. The solid line corresponds to a Standard Model prediction obtained from ALIBABA, adapted to the fit results given in Table 11

**Table 8.** Measured forward-backward asymmetry, $A_{FB}$, of the reaction $e^+e^- \to e^+e^-(\gamma)$. The asymmetry is determined from the number of events in the forward and backward hemispheres, not extrapolated to the full solid angle. Quoted errors are statistical only. The systematic error is estimated to be 0.01

| $\sqrt{s}$ (GeV) | $A_{FB}$ counting |
|---|---|
| 88.224 | $0.512 \pm 0.109$ |
| 89.227 | $0.372 \pm 0.077$ |
| 90.227 | $0.217 \pm 0.068$ |
| 91.222 | $0.102 \pm 0.023$ |
| 92.217 | $-0.039 \pm 0.078$ |
| 93.221 | $0.197 \pm 0.089$ |
| 94.215 | $0.155 \pm 0.136$ |

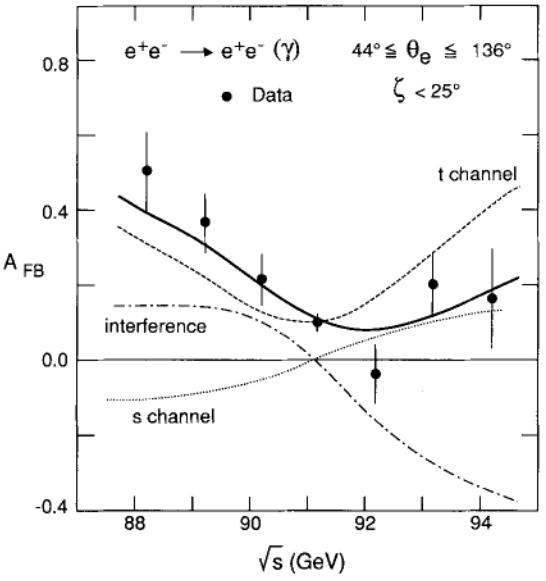


**Fig. 16.** The forward-backward asymmetry for $e^+e^- \to e^+e^-(\gamma)$ events as a function of $\sqrt{s}$. The solid line is a Standard Model prediction obtained from ALIBABA, adapted to the fit results given in Table 11. The separate $s, t$ and interference contributions are indicated

introduces a change in the asymmetry of $(0.07 \pm 0.01) \times A_{FB}$, which we correct for. The comparison of the momentum distributions of the positive and the negative muons in the forward and backward regions shows that in each hemisphere the acceptance is charge independent to better than 1%. Based on this, we conclude that the systematic error in the asymmetry of $e^+e^- \to e^+e^-(\gamma)$ is 0.01.

In Fig. 15 the differential cross section, at the $Z^0$ peak, is given as a function of $\cos\theta$. The data are corrected bin-by-bin for the selection efficiency and charge confusion. The asymmetry is defined by the difference between the forward $(44° < \theta < 90°)$ and backward $(90° < \theta < 136°)$ cross sections. In Table 8 the measured asymmetry is given at each energy point. In Fig. 16 the measured asymmetry is shown as a function of $\sqrt{s}$.

### *7.4 $Z^0$ resonance contribution to $e^+e^- \to e^+e^-(\gamma)$*

The $Z^0 \to e^+e^-(\gamma)$ cross section is composed of several contributions due to the $s$-channel and $t$-channel exchange of a $Z^0$ or a $\gamma$ and their interference. In lowest order of the electroweak theory, this gives a total of 10 terms. To extract $\Gamma_e$ the partial decay width for $Z^0 \to e^+e^-(\gamma)$, the normal method of $s$-channel fitting cannot be used directly.

The correct approach would be to compare the measured cross section to a theoretical prediction which includes all contributions. We exploit three available programs of this kind: Greco-Caffo-Remiddi (GCR) [17], ALIBABA [23] and a newly implemented program developed inside our collaboration, BHAGENE [24]. All three programs include $\mathcal{O}(\alpha)$ and $\mathcal{O}(\alpha^2)$ radiative corrections, and soft photons are accounted for by exponentiation. The GCR program includes hard photons only in the collinear approximation, while the other two programs numerically calculate their contribution.

An alternative method is to subtract the non-$s$-channel contributions from the measured cross section. This subtraction is done by evaluating the $t$-channel and the interference terms with the ALIBABA or BHAGENE program. The interference term depends on $\Gamma_e$, we therefore iterate the calculation of the terms to be subtracted. The procedure converges after 2 iterations, the systematic uncertainty due to this $\Gamma_e$ dependence of the interference term is negligible. In Fig. 14 we compare the measured cross section with the $s$-channel and the non-$s$-channel predictions and the sum of these two cross sections, as given by the ALIBABA program. After the subtraction of the non-$s$-channel contributions, the cross section can be fitted in the same way as for the other decay channels. The actual fitting is performed using the lineshape program ZFITTER [20], described in more detail in Sect. 8.3.

In Table 9 we compare $B_e$ the branching ratio of $Z^0 \to e^+e^-(\gamma)$ determined by the different methods described above. We obtain $B_e$ from a fit to the cross section data fixing the other relevant parameters of the Standard Model, i.e. $M_Z = 91.181$ GeV, $m_t = 150$ GeV, $M_H = 100$ GeV and $\alpha_s = 0.115$. From the comparison of these values, we assign a 0.4% theoretical systematic uncertainty to the determination of $B_e$. This corresponds to a 0.4% theoretical uncertainty in $\Gamma_e$, or a 0.8% systematic uncertainty in the peak cross section.

In Table 10 we give the $s$-channel cross section, $\sigma^s_{meas}$, after the subtraction of the $t$-channel and interference terms, using the ALIBABA program. At the $Z^0$ peak

**Table 9.** Branching ratio for the $Z^0 \to e^+e^-(\gamma)$ decay according to different fitting methods. The values in the first column are obtained from a fit to the complete cross section. The values in the second column are obtained from a fit, using ZFITTER, to the $s$-channel cross section only. The errors include statistical and systematic errors

| Program | $B_e$(%) | |
|---|---|---|
| | All terms | $s$-channel only ZFITTER |
| ALIBABA | $3.30 \pm 0.03$ | $3.32 \pm 0.03$ |
| BHAGENE | $3.30 \pm 0.03$ | $3.33 \pm 0.03$ |
| GCR | $3.32 \pm 0.03$ | |

**Table 10.** Results on the cross section and forward-backward asymmetry for the reaction $e^+e^- \to e^+e^-(\gamma)$ after the subtraction of the $t$-channel and interference contributions. $\sigma^s_{\text{meas}}$ is the corrected cross section for $44° < \theta < 136°$ and $\zeta < 25°$ and $\sigma^s_{\text{tot}}$ is the cross section extrapolated to the full solid angle. $A^s_{\text{FB}}$ is the forward-backward asymmetry in the angular range $44° < \theta < 136°$ and $\zeta < 25°$. Quoted errors are statistical only and the overall systematic uncertainty in $\sigma^s_{\text{meas}}$ is 1.0% and in $\sigma^s_{\text{tot}}$ is 1.1% (excluding the 0.9% luminosity uncertainty). The systematic uncertainty in $A^s_{\text{FB}}$ is 0.01%

| $\sqrt{s}$ (GeV) | $\sigma^s_{\text{meas}}$ (nb) | $\sigma^s_{\text{tot}}$ (nb) | $A^s_{\text{FB}}$ |
|---|---|---|---|
| 88.224 | $0.111 \pm 0.031$ | $0.190 \pm 0.053$ | $0.059 \pm 0.284$ |
| 89.227 | $0.290 \pm 0.035$ | $0.484 \pm 0.058$ | $-0.037 \pm 0.152$ |
| 90.227 | $0.609 \pm 0.050$ | $0.991 \pm 0.082$ | $-0.057 \pm 0.100$ |
| 91.222 | $0.893 \pm 0.019$ | $1.442 \pm 0.031$ | $-0.011 \pm 0.027$ |
| 92.217 | $0.671 \pm 0.042$ | $1.087 \pm 0.068$ | $-0.062 \pm 0.080$ |
| 93.221 | $0.414 \pm 0.029$ | $0.678 \pm 0.048$ | $0.184 \pm 0.091$ |
| 94.215 | $0.199 \pm 0.022$ | $0.329 \pm 0.036$ | $0.104 \pm 0.146$ |

the subtraction amounts to about 15%. The difference of the various approaches, combined with the 0.6% experimental systematic uncertainty discussed in Sect. 7.2, leads to a total systematic uncertainty of 1.0% in these cross sections (excluding the 0.9% uncertainty in the luminosity). For the comparison with the results from other experiments, we also give in Table 10 the $s$-channel cross section extrapolated to the full solid angle, $\sigma^s_{\text{tot}}$. The additional systematic uncertainty associated with this extrapolation is estimated to be 0.5%.

The same two methods (a direct fit to all channels and a fit after subtraction of the $t$-channel and the interference contributions) are also considered for the determination of the vector and the axial-vector couplings from the combined cross section and asymmetry measurements. The various methods give consistent results. We give in Table 10 the $s$-channel asymmetry, $A^s_{\text{FB}}$, obtained from a subtraction of the non-$s$-channel contributions with the ALIBABA program. In Fig. 16 the measured forward-backward asymmetries are compared to the ALIBABA predictions. The separate $s$, $t$ and interference contributions are also shown.

For consistency with the other $Z^0$ decay channels, we use in the simultaneous fit the $s$-channel data, obtained from the subtraction with the ALIBABA programm.

## 8 Determination of electroweak parameters

### *8.1 Electroweak parameters*

The cross section for the reaction $e^+e^- \to f\bar{f}$ to lowest order contains three terms, the $\gamma$ exchange, the $\gamma - Z^0$ interference and the $Z^0$ exchange term:

$$\sigma = \frac{4\pi\alpha^2}{3s}\left(Q_e^2 Q_f^2 - 2Q_e Q_f g_V^e g_V^f \operatorname{Re}\chi + |\chi|^2[(g_V^e)^2+(g_A^e)^2][(g_V^f)^2+(g_A^f)^2]\right), \tag{3}$$

with

$$\chi = \frac{\sqrt{2}G_\mu M_Z^2}{4\pi\alpha}\,\frac{s}{s - M_Z^2 + \mathrm{i}M_Z\Gamma_Z}. \tag{4}$$

Here $s$ is the center of mass energy squared, $M_Z$ is the mass, $\Gamma_Z$ is the total decay width of the $Z^0$ boson and $G_\mu$ is the Fermi constant determined from the muon lifetime. $Q_e$ and $Q_f$ are the charges of the electron and the fermion, respectively. The vector and axial-vector coupling constants, $g_V^f$ and $g_A^f$, are given by:

$$g_V^f = I_3^f - 2Q_f \sin^2\theta_W, \qquad g_A^f = I_3^f, \tag{5}$$

where $I_3^f$ is the third component of the weak isospin of the fermion and $\theta_W$ is the weak mixing angle. The cross section formula (3) is only valid in lowest order and fermion mass effects have been neglected. It is displayed here to introduce the relevant parameters. For the comparison of the measurements with the theoretical predictions, higher order electroweak radiative corrections must be taken into account as described below. Note also that for Bhabha scattering, $e^+e^- \to e^+e^-$, terms due to $t$-channel exchange must be added to (3).

The $Z^0$ exchange term in (3) is usually expressed in terms of the partial decay widths of the $Z^0$ into $e^+e^-$ and $f\bar{f}$:

$$\sigma(e^+e^- \to Z^0 \to f\bar{f}) = 12\pi\,\frac{\Gamma_e\Gamma_f}{M_Z^2}\,\frac{s}{(s-M_Z^2)^2 + M_Z^2\Gamma_Z^2}, \tag{6}$$

where $\Gamma_e$ is the partial decay width of $Z^0 \to e^+e^-$ and $\Gamma_f$ is the partial decay width of $Z^0 \to f\bar{f}$. Explicitly in lowest order:

$$\Gamma_f = \frac{G_\mu M_Z^3}{6\pi\sqrt{2}}\,[(g_V^f)^2 + (g_A^f)^2]. \tag{7}$$

The interference term in (3) cannot be expressed as a function of the partial widths $\Gamma_e$ and $\Gamma_f$. Thus additional assumptions must be made to extract the partial widths from the measured cross sections. However, the interference term is very small. It vanishes at the $Z^0$ peak and is less than 1.4% of the cross section for $0.20 < \sin^2\theta_W < 0.26$ at the extreme values of the energy range, $88.2 \leqq \sqrt{s} \leqq 94.2$ GeV. To extract the partial widths $\Gamma_e$ and $\Gamma_f$ or the corresponding branching ratios of the $Z^0$, we use the Standard Model expressions with $\sin^2\theta_W = 0.23$ for the vector couplings in the interference term. Changing the interference term between zero and twice the value predicted by the Standard Model for $\sin^2\theta_W = 0.23$, shifts the $Z^0$ mass by $\pm 3$ MeV. The error on the partial widths due to this approximation is negligible.

Additional constraints on the vector and axial-vector coupling constants can be obtained from the forward-backward asymmetry defined as

$$A_{\text{FB}} \equiv \frac{\sigma_F - \sigma_B}{\sigma_F + \sigma_B}, \tag{8}$$

where $\sigma_F$ is the cross section for events with a forward-going fermion, i.e. with the fermion polar angle $\theta$ with

respect to the electron beam direction less than 90°, and $\sigma_B$ is the cross section for events with backward-going fermions i.e. with $\theta > 90°$. The asymmetry is a strong function of the center of mass energy. Here we give the lowest order expression for the asymmetry at $\sqrt{s} = M_Z$:

$$A_{FB} = 3 \frac{g_V^e \cdot g_A^e}{(g_V^e)^2 + (g_A^e)^2} \frac{g_V^f \cdot g_A^f}{(g_V^f)^2 + (g_A^f)^2}. \quad (9)$$

Since the asymmetry and the cross sections depend on different combinations of the vector and axial-vector couplings, their simultaneous measurement provides a determination of these couplings. For the actual determination of the vector and axial-vector couplings we include higher order electroweak radiative corrections as described below. Consequently we do not determine the lowest order couplings $g_V$ and $g_A$ defined in (5), but the effective couplings, denoted by $\bar{g}_V$ and $\bar{g}_A$, as discussed in Sect. 8.3.

### *8.2 LEP beam energy*

The values of the center of mass energies are provided by the LEP machine group. By comparing the revolution frequency of protons and positrons, the absolute energy scale error is determined to be $\pm 0.02$ GeV [25].

The energy spread in the LEP beams yields an uncertainty in the center of mass energy for a given $e^+e^-$ collision of approximately 50 MeV [26]. We have determined the systematic effect of this uncertainty on the cross section for each decay channel by convoluting the $Z^0$ lineshape and a Gaussian $\sqrt{s}$ distribution with an r.m.s. value of 50 MeV. The corrections are small and change the cross section by 0.14% at the $Z^0$ peak and by less than 0.1% for the other energies. These corrections have been applied to the cross section data given in Sect. 4–7. The main effect of this correction is to reduce the width of the $Z^0$ by about 4 MeV.

### *8.3 Fitting procedure and radiative corrections*

Radiative corrections must be included in the theoretical predictions before they can be compared with our measurements of the hadronic and leptonic cross sections and the leptonic asymmetries. We use the analytical program ZFITTER [20] in conjunction with the MINUIT [27] program to fit the data and to determine the electroweak parameters.

ZFITTER uses analytical formulae to calculate cross sections, forward-backward asymmetries, and angular distributions of final state fermions in $e^+e^-$ interactions. It includes electroweak radiative corrections to $\mathcal{O}(\alpha)$ and a common exponentiation of initial and final state bremsstrahlung. Furthermore, the $\mathcal{O}(\alpha)$ corrections are supplemented with $\mathcal{O}(\alpha, \alpha_s)$ and leading $\mathcal{O}(\alpha^2 m_t^4 / M_W^4)$ corrections from $t$-quark insertions in the gauge boson self-energies.

We have made a detailed comparison of the results obtained with ZFITTER for the production cross sections of $e^+e^- \to f\bar{f}$ reactions and those obtained with another Standard Model program ZBATCH/ZHADRO [28]. We find that the cross sections calculated with the two programs agree within 0.5%. For $\mu^+\mu^-$ and $\tau^+\tau^-$ we have also compared the predictions of KORALZ [15] with ZFITTER and find that the cross sections calculated by these programs agree within 0.5%. Furthermore, we have compared the results of the lineshape fits of our data made by ZFITTER and the BCMS program [29], and we find excellent agreement for the same values of the electroweak parameters.

For the determination of the electroweak parameters from our measurements we proceed in the following way: we determine the mass, the total width and the different partial decay widths without restricting the range of these parameters to the Standard Model values. This is possible because the radiative corrections can be separated into QED corrections which take the real photon bremsstrahlung and the virtual photon loops into account, and the weak corrections, which involve vector boson propagators, vertex corrections and box diagrams with at least one vector boson exchanged [30, 31]. The QED corrections, which depend on the acceptance of the detector and on the cuts used in the analysis, are always taken into account for the calculation of the theoretical predictions. The weak corrections are not applied explicitly, but are absorbed in the definition of the fitted parameters. Thus we must interpret these parameters as being effective parameters. The use of effective parameters is also necessary for allowing these parameters to take values outside the Standard Model predictions in a fit to the data, because the weak radiative corrections cannot be calculated in this case. Similarly we determine in Sect. 8.7 effective values of the vector and axial-vector couplings which are there explicitly denoted by $\bar{g}_V$ and $\bar{g}_A$ to distinguish them from the one defined in (5).

The situation is different in Sect. 8.8 when one remains in the Standard Model framework with three lepton and quark families and only one Higgs doublet, and determines the unknown physical parameters appearing in this model, for example $M_Z$, $M_H$ and $m_t$. In this case the electroweak radiative corrections can be calculated exactly and they can be varied according to the values of the input parameters used.

Statistical, systematic, and overall normalization (luminosity) errors are included in all fit results that are presented in this section. The uncertainty of 0.02 GeV in the absolute energy scale of LEP must be added to the error on $M_Z$ [25].

### *8.4 Mass and partial decay widths of the $Z^0$*

We begin by simultaneously fitting the cross sections of $e^+e^- \to$ hadrons, $e^+e^-$, $\mu^+\mu^-$ and $\tau^+\tau^-$ to determine the following six parameters: $M_Z$, $\Gamma_Z$, $\Gamma_{had}$, $\Gamma_e$, $\Gamma_\mu$ and $\Gamma_\tau$. As mentioned above, we use for the $e^+e^- \to$ hadrons, $\mu^+\mu^-$ and $\tau^+\tau^-$ channels the cross sections extrapolated to the full solid angle. For the $e^+e^- \to e^+e^-$ channel we use the $s$-channel cross sections in the $44° < \theta < 136°$ polar angular range and with $\zeta < 25°$, excluding the points at $\sqrt{s} = 88.224$ GeV and

$\sqrt{s} = 94.215$ GeV because of large $t$-channel corrections. The results obtained from the fit are presented in Table 11 together with the expected Standard Model values for $M_Z = 91.181$ GeV, $m_t = 150$ GeV, $M_H = 100$ GeV and $\alpha_s = 0.115$. The fit has a $\chi^2$ of 18 for 20 degrees of freedom. Our measurements of the total and partial decay widths of the $Z^0$ agree very well with the Standard Model predictions using these parameters. The partial decay widths of the electron, muon and tau are equal within

**Table 11.** Results obtained from the fits to the cross section data. The four-parameter fit assumes lepton universality while the six-parameter fit does not. Standard Model expectations are presented for $M_Z = 91.181$ GeV. All errors include statistical and systematic errors. The uncertainty of 0.02 GeV in the absolute energy scale of LEP must be added to the error on $M_Z$

| Parameter | Fit results | | Standard Model |
|---|---|---|---|
| | 6 parameters | 4 parameters | |
| $M_Z$ (GeV) | $91.181 \pm 0.010$ | $91.181 \pm 0.010$ | |
| $\Gamma_Z$ (MeV) | $2501 \pm 17$ | $2501 \pm 17$ | 2490 |
| $\Gamma_{had}$ (MeV) | $1749 \pm 24$ | $1742 \pm 19$ | 1738 |
| $\Gamma_e$ (MeV) | $83.3 \pm 1.1$ | | 83.8 |
| $\Gamma_\mu$ (MeV) | $84.5 \pm 2.0$ | | 83.8 |
| $\Gamma_\tau$ (MeV) | $84.0 \pm 2.7$ | | 83.6 |
| $\Gamma_l$ (MeV) | | $83.6 \pm 0.8$ | 83.7 |

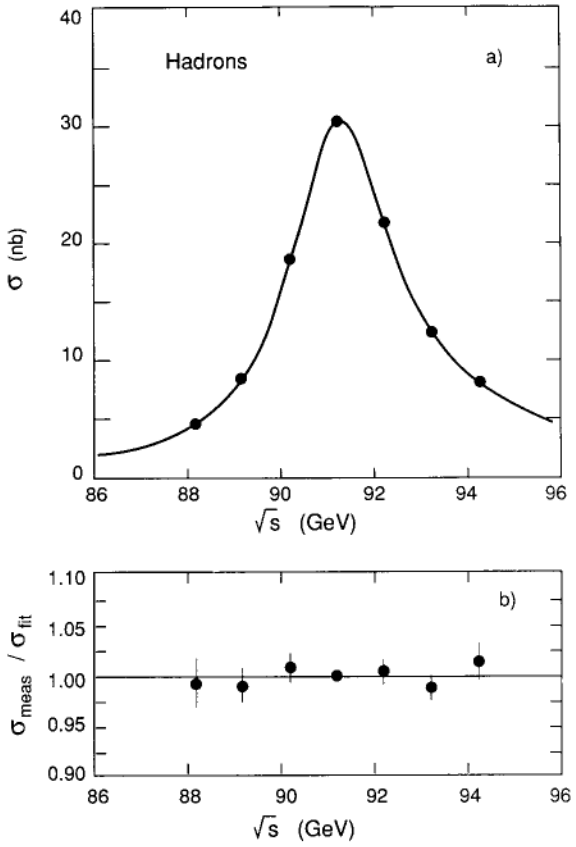


**Fig. 17a, b.** **a** The cross section for $e^+e^- \to$ hadrons as a function of $\sqrt{s}$. The solid curve is the result of the four-parameter fit (Table 11) assuming lepton universality. **b** The cross section ratio of the measured value to the fitted value as a function of $\sqrt{s}$ for $e^+e^- \to$ hadrons

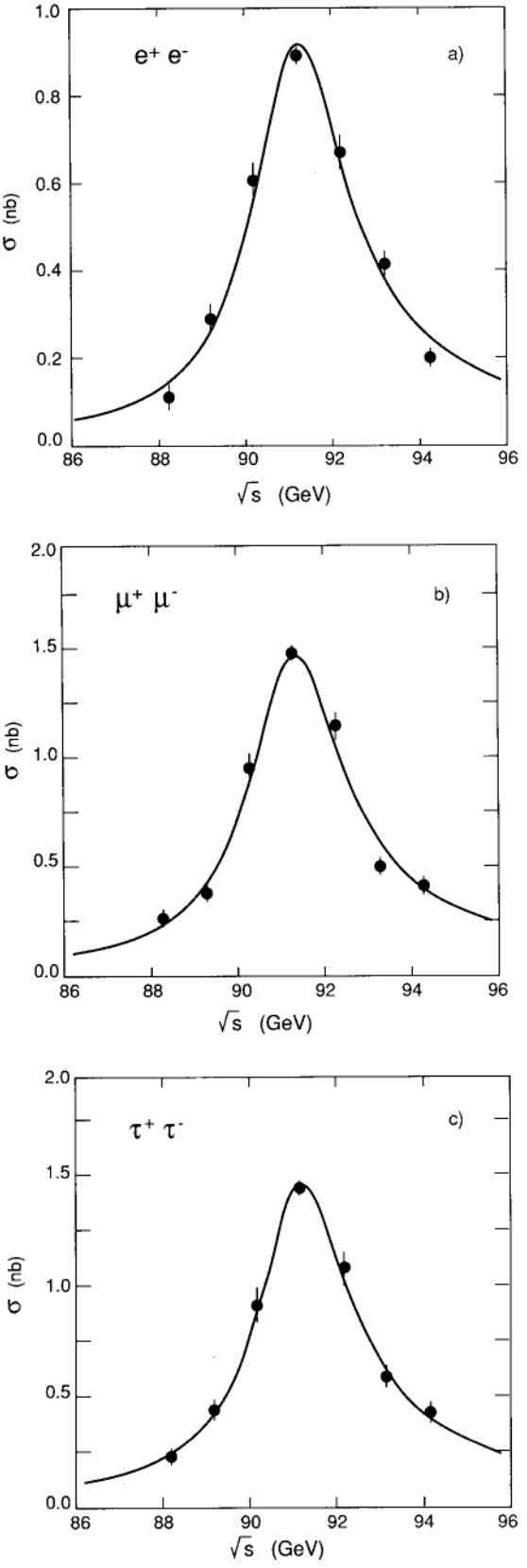


**Fig. 18a–c.** **a** The $s$-channel cross section in the angular range $44° < \theta < 136°$ and with $\zeta < 25°$ for $e^+e^- \to e^+e^-$, **b** the cross section for $e^+e^- \to \mu^+\mu^-$, corrected for geometrical acceptance, and **c** the cross section for $e^+e^- \to \tau^+\tau^-$, corrected for geometrical acceptance, as a function of $\sqrt{s}$. The solid curves are the results of the four-parameter fit (Table 11) assuming lepton universality

errors and confirm the lepton universality of the weak neutral current interaction predicted by the Standard Model.

Next, we assume lepton universality and perform a four-parameter fit to the measured cross section results to determine $M_Z$, $\Gamma_Z$, $\Gamma_{had}$ and the leptonic decay width $\Gamma_l$. The $\chi^2$ of this fit is 19 for 22 degrees of freedom. Results of the fit are also given in Table 11. This fit leads to a measurement of the leptonic width with a precision of 1%. The results for the mass and the total width of the $Z^0$ remain the same, while the error on the hadronic width is reduced. Figure 17 shows our measurements of the hadronic cross section, and Fig. 18 shows our measurements for the three leptonic cross sections. The data are compared to the theoretical predictions using the parameters determined by the fit with lepton universality. The agreement is very good in all four reactions.

The mass and the total decay width of the $Z^0$ are mainly determined by the shape of the hadronic cross section, due to the low statistical and systematic errors for this channel. The partial decay widths into hadrons, electrons, muons and taus are mainly measured from the peak cross section of each reaction. The lowest order cross section at $\sqrt{s}=M_Z$, $\sigma^0_{peak}$, of the reaction $e^+e^-\to f\bar{f}$ is directly related to the product of the branching ratios, $B_e$ and $B_f$, of $Z^0\to e^+e^-$ and $Z^0\to f\bar{f}$:

$$\sigma^0_{peak}=\frac{12\pi}{M_Z^2}\frac{\Gamma_e\Gamma_f}{\Gamma_Z^2}=\frac{12\pi}{M_Z^2}B_eB_f. \tag{10}$$

We can determine the different branching ratios instead of the partial widths. The results are shown in Table 12 for fits with and without the lepton universality assumption. We also give the lowest order peak cross section ($\sigma^0_{peak}$) calculated from (10).

### 8.5 Number of light neutrino species

We use the results of the fit presented in Table 11 and the correlations between the fitted parameters to determine the invisible width of the $Z^0$:

$$\Gamma_{inv}\equiv\Gamma_Z-\Gamma_{had}-3\Gamma_l=508\pm17\ \text{MeV}. \tag{11}$$

**Table 12.** Peak cross sections, corrected for radiative effects, and branching ratios obtained from the fits to the cross section data. The $e^+e^-$, $\mu^+\mu^-$ and $\tau^+\tau^-$ peak cross section results are taken from the fit without the lepton universality assumption. All errors include statistical and systematic errors. The measured branching ratios are compared to the Standard Model predictions

| Decay | $\sigma^0_{peak}$ (nb) | Branching ratio (%) | | |
|---|---|---|---|---|
| | | No lepton universality | Lepton universality | Standard Model |
| $Z^0\to$hadrons | 41.1 ±0.4 | 69.9 ±0.9 | 69.7 ±0.7 | 69.8 |
| $Z^0\to e^+e^-$ | 1.96±0.05 | 3.33±0.04 | | 3.36 |
| $Z^0\to\mu^+\mu^-$ | 1.99±0.04 | 3.38±0.08 | | 3.36 |
| $Z^0\to\tau^+\tau^-$ | 1.97±0.06 | 3.36±0.11 | | 3.36 |
| $Z^0\to l^+l^-$ | 1.97±0.03 | | 3.34±0.03 | 3.36 |

We use the following relation to determine the number of light neutrino species:

$$N_\nu=\frac{\Gamma_{inv}}{\Gamma_l}\left(\frac{\Gamma_l}{\Gamma_\nu}\right)^{SM}, \tag{12}$$

where the superscript SM denotes the Standard Model prediction. The ratio of $(\Gamma_l/\Gamma_\nu)^{SM}$ is insensitive to $m_t$ and $M_H$ and has the value 0.502 for $M_Z=91.181$ GeV. Using the above value of $\Gamma_{inv}$ and our measurement of $\Gamma_l$ (taking into account their correlations), we obtain:

$$N_\nu=3.05\pm0.10.$$

The error is to a large extent due to the systematic error in the luminosity measurement.

### 8.6 QCD correction and strong coupling constant

The hadronic decay width of the $Z^0$ can be expressed as:

$$\Gamma_{had}=\Gamma^0_{had}(1+\delta_{QCD})$$
$$=\Gamma^0_{had}\left(1+\frac{\alpha_s}{\pi}+1.4\left(\frac{\alpha_s}{\pi}\right)^2+\dots\right), \tag{13}$$

where $\Gamma^0_{had}$ is the Standard Model prediction for $\alpha_s=0$ and $\delta_{QCD}$ is a QCD correction factor [32]. We prefer to use the $m_t$ independent ratio of the hadronic to the leptonic width for a comparison with the Standard Model prediction:

$$R_{had}\equiv\frac{\Gamma_{had}}{\Gamma_l}=R^0_{had}(1+\delta_{QCD}). \tag{14}$$

Here again $R^0_{had}$ denotes the Standard Model prediction for this ratio with $\alpha_s=0$. We obtain $R^0_{had}=20.00\pm0.03$ from the program ZFITTER for $M_Z=91.181$ GeV. The uncertainty accounts for variations of $m_t$ and $M_H$ over a wide range. From the results for $\Gamma_{had}$ and $\Gamma_l$ presented in Table 11 and the correlations between the fitted parameters, we obtain $R_{had}=20.84\pm0.29$. This gives a QCD correction factor of $\delta_{QCD}=0.042\pm0.015$, which corresponds to a value of the strong coupling constant $\alpha_s=0.125\pm0.041$.

Alternatively, we can use our measurements [33] of $\alpha_s$ from jet multiplicities and the asymmetry of the energy-energy correlation, $\alpha_s=0.115\pm0.009$, to obtain the Standard Model prediction for $R^{SM}_{had}=20.77\pm0.10$. Since $R^{SM}_{had}$ is a ratio of the partial widths, it is insensitive to variations of $m_t$ and $M_H$. Thus, a comparison of this value with our measurement is a strong test of the Standard Model because there are no unknown parameters involved. We find a very good agreement:

$$\frac{R_{had}}{R^{SM}_{had}}=1.003\pm0.015.$$

### 8.7 Neutral current coupling constants $\bar{g}_V$ and $\bar{g}_A$

We perform a simultaneous fit to the measured cross sections of $e^+e^-\to$hadrons, $e^+e^-$, $\mu^+\mu^-$ and $\tau^+\tau^-$,

**Table 13.** Results obtained from a combined fit to the cross section and forward-backward asymmetry data. Standard Model expectations are presented for $M_Z = 91.181$ GeV. Errors include statistical and systematic errors, except the 0.02 GeV LEP energy uncertainty

| Parameter | Fit result | Standard Model |
|---|---|---|
| $M_Z$ (GeV) | $91.181 \pm 0.010$ | |
| $\Gamma_Z$ (MeV) | $2501 \pm 17$ | 2490 |
| $\Gamma_{had}$ (MeV) | $1742 \pm 19$ | 1738 |
| $\bar{g}_A$ | $-0.500 \pm 0.003$ | $-0.501$ |
| $\bar{g}_V$ | $-0.046^{+0.015}_{-0.012}$ | $-0.035$ |

and to the leptonic forward-backward asymmetries to determine $M_Z$, $\Gamma_Z$, $\Gamma_{had}$, $\bar{g}_V$ and $\bar{g}_A$, assuming lepton universality. For the asymmetries of the $e^+e^- \to \mu^+\mu^-$ and $\tau^+\tau^-$ channels, we use the results from the maximum likelihood method. For the asymmetry of the $e^+e^- \to e^+e^-$ channel we use the $s$-channel asymmetry in the $44° < \theta < 136°$ polar angular range and $\zeta < 25°$, excluding the points at $\sqrt{s} = 88.224$ GeV and $\sqrt{s} = 94.215$ GeV because of large $t$-channel corrections. Results obtained from the fit are presented in Table 13. In Fig. 19 our measurements of the forward-backward asymmetries are compared with the theoretical predictions using the parameters determined by the fit. The fit has a $\chi^2$ of 34 for 40 degrees of freedom. The values obtained for $M_Z$, $\Gamma_Z$, and $\Gamma_{had}$ are identical to those that were obtained in Sect. 8.4. The signs of $\bar{g}_V$ and $\bar{g}_A$ have been inferred from the results of other experiments [34]. Figure 20 shows the 68% and 95% confidence level contours in the $\bar{g}_V$ and $\bar{g}_A$ plane.

We have also repeated the fit to the data to determine the values for $\sin^2\bar{\theta}_W$ and $\rho_{eff}$, which are related to $\bar{g}_V$ and $\bar{g}_A$ through the following relations [30]:

$$\bar{g}_A = -0.5\sqrt{\rho_{eff}}\,,$$
$$\bar{g}_V = -0.5\sqrt{\rho_{eff}}(1 - 4\sin^2\bar{\theta}_W)\,. \qquad (15)$$

The values of $\sin^2\bar{\theta}_W$ and $\rho_{eff}$ are:

$$\sin^2\bar{\theta}_W = 0.227^{+0.008}_{-0.006}\,,$$
$$\rho_{eff} = 1.000 \pm 0.011\,.$$

It should be noted that the results on $\bar{g}_V$ and $\bar{g}_A$, or $\sin^2\bar{\theta}_W$ and $\rho_{eff}$, are obtained from fits where these parameters can assume values which deviate from the ones allowed in the minimal Standard Model.

To test lepton universality, it would be very interesting to extract the vector and the axial-vector couplings of the electron, muon and tau from a fit without the lepton universality assumption. However, the asymmetry of $e^+e^- \to \mu^+\mu^-$ or $e^+e^- \to \tau^+\tau^-$ measures the product of $\bar{g}_V^e \cdot \bar{g}_V^\mu$ or $\bar{g}_V^e \bar{g}_V^\tau$, respectively. If the vector coupling of the electron is very small, as it is for $\sin^2\bar{\theta}_W = 0.23$, the asymmetry is insensitive to the muon or tau coupling. Thus, these couplings cannot be measured with reasonable errors using the current statistics. It is possible to extract the vector and axial-vector couplings of the electron from

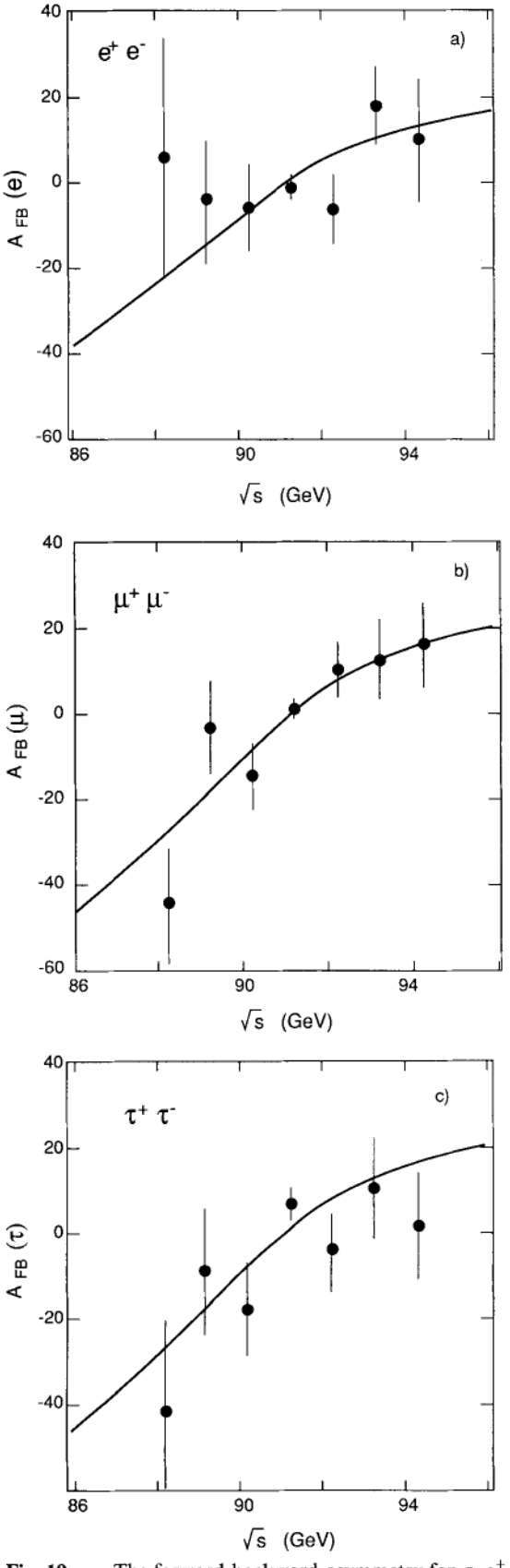


**Fig. 19a–c.** The forward-backward asymmetry for **a** $e^+e^- \to e^+e^-$ in the $44° < \theta < 136°$ angular range and with $\zeta < 25°$, **b** $e^+e^- \to \mu^+\mu^-$, and **c** $e^+e^- \to \tau^+\tau^-$ events as a function of $\sqrt{s}$. The solid curves represent the fit with the parameters given in Table 13

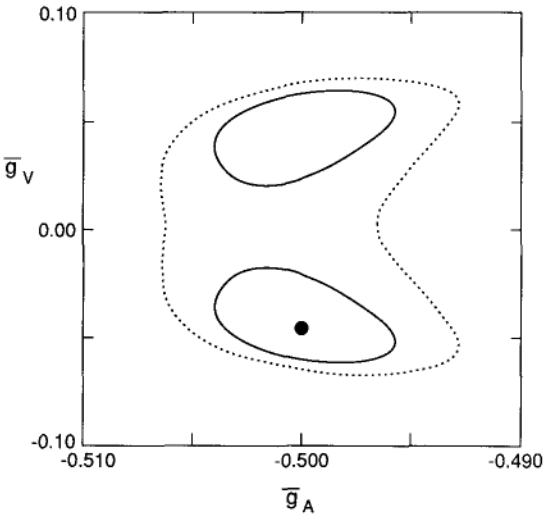


**Fig. 20.** Values of $\bar{g}_V$ and $\bar{g}_A$ obtained from a fit to the hadronic and leptonic cross sections and leptonic forward-backward asymmetries. The contours shown represent the 68% (solid) and the 95% (dotted) confidence level limits. The point indicates the solution preferred by the neutrino experiments [34]

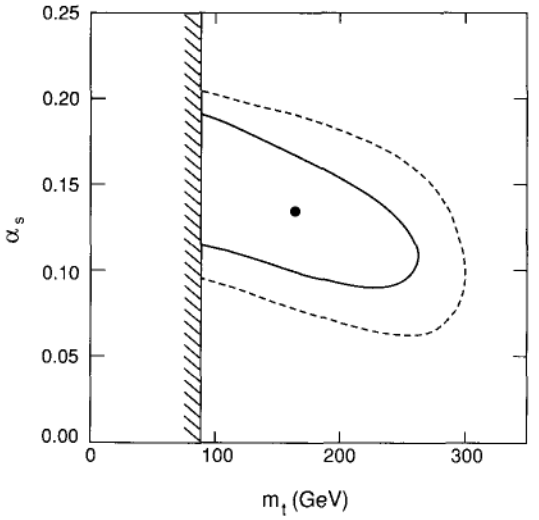


**Fig. 21.** Values of $m_t$ and $\alpha_s$ obtained from a fit to the hadronic and leptonic cross sections and leptonic forward-backward asymmetries. The contours shown represent the 68% (solid) and the 95% (dotted) confidence level limits. The shaded region corresponds to the upper limit from the CDF experiment [35]. The point indicates the best fit values. The Higgs mass is fixed to 300 GeV

a fit to the electron data. This is because in the electron case we measure $(\bar{g}_V^e)^2$ and $(\bar{g}_A^e)^2$. We include in this fit the hadron data which are needed for a precise determination of the mass and total width of the $Z^0$. The result of this fit gives:

$$\bar{g}_A^e = -0.501^{+0.004}_{-0.003},$$
$$\bar{g}_V^e = -0.008^{+0.060}_{-0.044}.$$

The signs of the vector and axial-vector couplings are inferred from the results of other experiments [34]. The mass, the total width and the hadronic decay width of the $Z^0$ are identical to the ones given in Table 13.

### *8.8 Mass of the top quark and $\sin^2\theta_W$*

In the absence of direct experimental evidence for the top quark [35], its mass can be indirectly estimated within the framework of the Standard Model by using the sensitivity of radiative corrections to $m_t$. An estimate of $m_t$ can be obtained from a combined fit to all of the cross section and forward-backward asymmetry data within the Standard Model, since the total and partial decay widths of the $Z^0$ and the leptonic forward-backward asymmetries depend on $m_t$.

We fit the data with $M_Z$, $m_t$ and $\alpha_s$ as free parameters. As discussed below the results depend only weakly on the Higgs mass which we therefore fix to $M_H = 300$ GeV. Figure 21 indicates the best fit values and the 68% and the 95% confidence level contours in the $\alpha_s - m_t$ plane. We obtain

$$\alpha_s = 0.134 \pm 0.030,$$
$$m_t = 165^{+70}_{-110}\ \text{GeV}.$$

The $Z^0$-mass remains at the value given in Table 11. The error on $\alpha_s$ is smaller than the one given in Sect. 8.6 because we use all measurements and not only $R_{\text{had}}$.

We can decrease the error on $m_t$ by constraining $\alpha_s$ to $\alpha_s = 0.115 \pm 0.009$ determined by our measurements of the energy-energy correlation asymmetry and of the jet multiplicities [33]. To take into account the uncertainty due to the unknown Higgs mass, we vary $M_H$ between 50 and 1000 GeV. Results of the fits are presented in Table 14. The fitted values of $M_Z$ are found to be identical to those given in Table 11. For all the fits, a $\chi^2$ of 36 for 43 degrees of freedom is obtained. We quote the central value obtained for $M_H = 300$ GeV as our result:

$$m_t = 193^{+52}_{-69} \pm 16\ (\text{Higgs})\ \text{GeV}.$$

The second error takes into account the variation of the Higgs mass from 50 to 1000 GeV.

From the measurement of $m_t$, for a fixed value of $M_H$, we can derive the radiative correction factor $\Delta r$ or the weak mixing angle $\sin^2\theta_W$ or the mass of the $W$ boson $M_W$. These quantities are related as follows:

$$M_W^2 \sin^2\theta_W = \frac{\pi\alpha}{\sqrt{2}\,G_\mu(1-\Delta r)}, \qquad \sin^2\theta_W \equiv 1 - M_W^2/M_Z^2. \tag{16}$$

The values of $\Delta r$, $\sin^2\theta_W$ and $M_W$ are shown in Table 14 for different values of $M_H$. Although the top quark mass determined from our measurements shows a dependence on the Higgs mass, the values of $\Delta r$, $\sin^2\theta_W$ and $M_W$ are practically independent of $M_H$, as can be seen from Table 14. We obtain $\sin^2\theta_W \equiv 1 - \dfrac{M_W^2}{M_Z^2} = 0.222 \pm 0.008$, corre-

**Table 14.** Combined fit to cross section and forward-backward asymmetry data in order to determine $M_Z$ and $m_t$ as a function of $M_H$. The derived quantities $\Delta r$, $\sin^2\theta_W$, and $M_W$ are also given

| Parameter | $M_H$ (GeV) | | | |
|---|---|---|---|---|
| | 50 | 100 | 300 | 1000 |
| $M_Z$ (GeV) | $91.181 \pm 0.010$ | $91.181 \pm 0.010$ | $91.181 \pm 0.010$ | $91.181 \pm 0.010$ |
| $m_t$ (GeV) | $179^{+55}_{-76}$ | $182^{+54}_{-74}$ | $193^{+52}_{-69}$ | $209^{+49}_{-63}$ |
| $\Delta r$ | $0.030 \pm 0.026$ | $0.031 \pm 0.026$ | $0.030 \pm 0.025$ | $0.029 \pm 0.025$ |
| $\sin^2\theta_W$ | $0.222 \pm 0.009$ | $0.222 \pm 0.008$ | $0.222 \pm 0.008$ | $0.222 \pm 0.008$ |
| $M_W$ (GeV) | $80.44 \pm 0.46$ | $80.43 \pm 0.45$ | $80.44 \pm 0.45$ | $80.46 \pm 0.44$ |

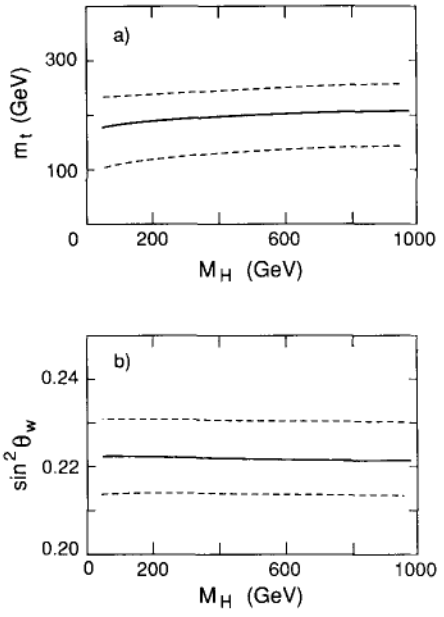


**Fig. 22a, b.** **a** The fitted values of $m_t$ as a function of $M_H$. **b** The fitted values of $\sin^2\theta_W$ as a function of $M_H$. The solid lines are the central values of the fit to all hadronic and leptonic measurements. The dashed lines indicate the $\pm 1$ sigma error bands

sponding to the effective weak mixing angle $\sin^2\bar{\theta}_W = 0.2315 \pm 0.0025$. This value of $\sin^2\bar{\theta}_W$ is in good agreement with our independent determination $\sin^2\bar{\theta}_W = 0.226 \pm 0.008$ from the forward-backward asymmetry of $Z^0 \to b\bar{b}$ events [36]. The variations of $m_t$ and $\sin^2\theta_W$ as a function of $M_H$ are shown in Fig. 22.

An independent measurement of $\sin^2\theta_W$ has been made at $p\bar{p}$ colliders [37]. The value of $\sin^2\theta_W = 0.227 \pm 0.006$ can be compared with our value of $\sin^2\theta_W = 0.222 \pm 0.008$. Repeating our fitting procedure, constraining $\sin^2\theta_W$ to the $p\bar{p}$ result, we obtain: $m_t = 164^{+37}_{-44} \pm 16$ (Higgs) GeV.

## 9 Conclusions

We have measured the reactions $e^+e^- \to$ hadrons, $e^+e^-$, $\mu^+\mu^-$ and $\tau^+\tau^-$ at LEP in the energy range $88.2 \leqq \sqrt{s} \leqq 94.2$ GeV, around the $Z^0$ resonance. A total luminosity of 5.5 pb$^{-1}$ has been recorded with the L3 detector corresponding to the following final event sample:

115097 $e^+e^- \to$ hadrons events,

4175 $e^+e^- \to e^+e^-(\gamma)$ events,

3245 $e^+e^- \to \mu^+\mu^-(\gamma)$ events,

2540 $e^+e^- \to \tau^+\tau^-(\gamma)$ events.

A good understanding of the detector leads to low systematic errors, thus permitting us to use the full potential of the high statistics data.

A combined fit to all reactions gives the following values of the $Z^0$ parameters:

$M_Z = 91.181 \pm 0.010 \pm 0.02$ (LEP) GeV,

$\Gamma_Z = 2501 \pm 17$ MeV,

$\Gamma_{\text{had}} = 1742 \pm 19$ MeV,

$\Gamma_e = 83.3 \pm 1.1$ MeV,

$\Gamma_\mu = 84.5 \pm 2.0$ MeV,

$\Gamma_\tau = 84.0 \pm 2.7$ MeV,

$\Gamma_l = 83.6 \pm 0.8$ MeV,

$\Gamma_{\text{inv}} = 508 \pm 17$ MeV.

From our measured ratio of $\Gamma_{\text{inv}}/\Gamma_l$ we extract for the number of light neutrino species:

$N_\nu = 3.05 \pm 0.10$.

Including the measurements of the forward-backward asymmetry, we determine the vector and axial-vector neutral current coupling constants of charged leptons to the $Z^0$ to be:

$\bar{g}_V = -0.046^{+0.015}_{-0.012}$,

$\bar{g}_A = -0.500 \pm 0.003$.

Fitting all of our data in the framework of the Standard Model with $N_\nu = 3$ and $\alpha_s = 0.115 \pm 0.009$, we determine the mass of the top quark:

$m_t = 193^{+52}_{-69} \pm 16$ (Higgs) GeV.

Alternatively, we can derive a value of the $W$ mass

$M_W = 80.44 \pm 0.45$ GeV

or, expressed in terms of the weak mixing angle,

$$\sin^2\theta_W \equiv 1 - \frac{M_W^2}{M_Z^2} = 0.222 \pm 0.008$$

which corresponds to the following value of the effective weak mixing angle:

$$\sin^2 \bar{\theta}_W = 0.2315 \pm 0.0025 .$$

These results are independent of the Higgs mass for $50 < M_H < 1000$ GeV.

All our results are in good agreement with the predictions of the Standard Model, with the results from neutrino experiments [38] and with the other measurements at LEP, SLC and the $p\bar{p}$ colliders [6, 39, 37].

*Acknowledgements.* We wish to thank CERN for its hospitality and help. We want particularly to express our gratitude to the LEP division: it is their excellent achievements which made this experiment possible.

## References

1. S.L. Glashow: Nucl. Phys. 22 (1961) 579; S. Weinberg: Phys. Rev. Lett. 19 (1967) 1264; A. Salam: Elementary particle theory, p. 367, N. Svartholm (ed.). Stockholm: Almquist and Wiksell 1968
2. LEP Design Report, CERN-LEP/84-01, June 1984; S. Meyers: The Performance of LEP and Future Developments, invited paper to the 2nd European Particle Accelerator Conference, Nice, 1990; Vol. 1, pages 13–19
3. L3 Coll., B. Adeva et al.: Phys. Lett. B231 (1989) 509; L3 Coll., B. Adeva et al.: Phys. Lett. B236 (1990) 109; L3 Coll., B. Adeva et al.: Phys. Lett. B237 (1990) 136; L3 Coll., B. Adeva et al.: Phys. Lett. B238 (1990) 122; L3 Coll., B. Adeva et al.: Phys. Lett. B247 (1990) 473
4. L3 Coll., B. Adeva et al.: Phys. Lett. B249 (1990) 341
5. L3 Coll., B. Adeva et al.: Phys. Lett. B250 (1990) 183
6. ALEPH Coll., D. Decamp et al.: Phys. Lett. B231 (1989) 519; ALEPH Coll., D. Decamp et al.: Phys. Lett. B234 (1990) 399; ALEPH Coll., D. Decamp et al.: Phys. Lett. B235 (1990) 399; ALEPH Coll., D. Decamp et al.: Z. Phys. C – Particles and Fields 48 (1990) 365;
   DELPHI Coll., P. Aarnio et al.: Phys. Lett. B231 (1989) 539; DELPHI Coll., P. Aarnio et al.: Phys. Lett. B241 (1990) 425; DELPHI Coll., P. Abreu et al.: Phys. Lett. B241 (1990) 435;
   OPAL Coll., M.Z. Akrawy et al.: Phys. Lett. B231 (1989) 530; OPAL Coll., M.Z. Akrawy et al.: Phys. Lett. B235 (1990) 379; OPAL Coll., M.Z. Akrawy et al.: Phys. Lett. B240 (1990) 497; OPAL Coll., M.Z. Akrawy et al.: Phys. Lett. B247 (1990) 458
7. L3 Coll., B. Adeva et al.: Nucl. Instrum. Methods A289 (1990) 35
8. R. Brun et al.: GEANT 3 Users Guide, CERN/DD/EE/84.1
9. H. Fesefeldt: RWTH Aachen Report PITHA 85/02 (1985)
10. M. Böhm, A. Denner, W. Hollik: Nucl. Phys. B304 (1988) 687; F.A. Berends, R. Kleiss, W. Hollik: Nucl. Phys. B304 (1988) 712
11. S. Jadach, B.F.L. Ward: Phys. Rev. D40 (1989) 3582
12. F.A. Berends, R. Kleiss: Nucl. Phys. B186 (1981) 22
13. T. Sjöstrand, M. Bengtsson: Comput. Phys. Commun. 43 (1987) 367; T. Sjöstrand: Z Physics at LEP 1, G. Altarelli et al. (eds.), CERN Report CERN-89-08, Vol. 3 (1989) 143
14. G. Marchesini, B. Webber: Nucl. Phys. B310 (1988) 461
15. S. Jadach et al.: Z Physics at LEP 1, G. Altarelli et al. (eds.), CERN Report CERN-89-08, Vol. 3 (1989) 69
16. F.A. Berends, P.H. Daverveldt, R. Kleiss:Nucl. Phys. B253 (1985) 441
17. M. Caffo, E. Remiddi, F. Semeria: Z Physics at LEP 1, G. Altarelli et al. (eds.), CERN Report CERN-89-08, Vol. 1 (1989) 171
18. W. Beenakker, F.A. Berends, S.C. van der Marck: Small angle Bhabha scattering, Leiden preprint 1990
19. O. Adriani et al.: Nucl. Instrum. Methods A302 (1991) 53
20. D. Bardin et al.: Nucl. Phys. B351 (1991) 1; D. Bardin et al.: Z. Phys. C – Particles and Fields 44 (1989) 493; D. Bardin et al.: Phys. Lett. B255 (1991) 290; M. Bilenky, A. Sazonov: JNIR Dubna preprint E2-89-792 (1989) unpublished
21. L3 Coll., B. Adeva et al.: Phys. Lett. B250 (1990) 199
22. M. Greco: Phys. Lett. B177 (1986) 97; M. Greco: Riv. Nuovo Cimento 11 (1988) 1; F. Aversa et al.: LNF-90/049 (1990)
23. W. Beenakker, F.A. Berends, S.C. van der Marck: Large angle Bhabha scattering, and Higher order corrections to the forward-backward asymmetry, Leiden preprints 1990; W. Beenakker, W. Hollik: ECFA workshop on LEP 200, A. Böhm et al. (eds.), CERN Report CERN-87-08 (1987) 185; W. Hollik: DESY Report DESY-88-188 (1988)
24. BHAGENE, a Monte Carlo event genarator for wide angle Bhabha scattering, incorporating initial and final state exponentiation. J.H. Field and T. Riemann, private communications
25. V. Hatton et al.: LEP Absolute Energy in 1990, LEP performance note 12
26. A. Hoffman: private communication
27. F. James, M. Roos: MINUIT manual, CERN-D506 (1989)
28. G. Burgers: CERN preprint CERN-TH-5119/88 (1988)
29. A. Borrelli et al.: Nucl. Phys. B333 (1990) 357
30. M. Consoli, W. Hollik: Z Physics at LEP 1, G. Altarelli et al. (eds.), CERN Report CERN-89-08, Vol.1 (1989) 7; M. Böhm, W. Hollik: Z Physics at LEP 1, G. Altarelli et al. (eds.), CERN Report CERN-89-08, Vol. 1 (1989) 203
31. W. Hollik: Fortschr. Phys. 38 (1990) 165
32. K.G. Chetyrkin, A.L. Kataev, F.V. Tkachov: Phys. Lett. B85 (1979) 277; M. Dine, J. Sapirstein: Phys. Rev. Lett. 43 (1979) 668; W. Celmaster, R.J. Gonsalves: Phys. Rev. Lett. 44 (1980) 560; Phys. Rev. D21 (1980) 3112
33. L3 Coll., B. Adeva et al.: Phys. Lett. B248 (1990) 464; L3 Coll., B. Adeva et al.: Phys. Lett. B257 (1991) 469
34. CHARM Coll., J. Dorenbosch et al.: Z. Phys. C – Particles and Fields (1989) 567; K. Abe et al.: Phys. Rev. Lett. 62 (1989) 1709; CHARM II Coll., D. Geiregat et al.: Phys. Lett. B232 (1989) 539; F. Avignone et al.: Phys. Rev. D16 (1977) 2383; U. Amaldi et al.: Phys. Rev. D36 (1987) 1385
35. K. Sliwa (CDF Coll.: In: Proc. 25th Rencontre de Moriond: Hadronic Interactions, Les Arcs, 1990. Gif-sur-Yvette: Editions Frontières
36. L3 Coll., B. Adeva et al.: Phys. Lett. B252 (1990) 713
37. CDF Coll., F. Abe et al.: Phys. Rev. Lett. 65 (1990) 2243; UA2 Coll., J. Alitti et al.: Phys. Lett. B241 (1990) 150
38. CHARM Coll., J.V.Allaby et al.: Z. Phys. C – Particles and Fields 36 (1987) 611; CDHSW Coll., H. Abramowicz et al.: Phys. Rev. Lett. 57 (1986) 298; CDHSW Coll., A. Blondel et al.: Z. Phys. C – Particles and Fields 45 (1990) 361; CCFR Coll., P. G. Reutens et al.: Z. Phys. C – Particles and Fields 45 (1990) 539; CHARM Coll., J. Dorenbosch et al.: Z. Phys. C – Particles and Fields 41 (1989) 567; CHARM II Coll., D. Geiregat et al.: CERN preprint CERN-PPE/91-15 to be published in Phys. Lett. B; L. A. Ahrens et al.: Phys. Rev. D41 (1990) 3297
39. Mark II Coll., S. Komamiya et al.: Phys. Rev. Lett. 63 (1989) 724; Mark II Coll., G.S. Abrams et al.: Phys. Rev. Lett. 63 (1989) 2173 and 2781